Extreme Ozone Loss Following Nuclear War Results in Enhanced Surface Ultraviolet Radiation

Charles G. Bardeen[1], Douglas E. Kinnison[1], Owen B. Toon[2], Michael J. Mills[1], Francis Vitt[1], Lili Xia[3], Jonas Jägermeyr[4,5,6], Nicole S. Lovenduski[7], Kim J. N. Scherrer[8], Margot Clyne[2], and Alan Robock[3]

[1] National Center for Atmospheric Research, Boulder, CO, USA

[2] Laboratory for Atmospheric and Space Physics and Department of Atmospheric and Ocean Sciences, University of Colorado, Boulder, CO, USA

[3] Department of Environmental Sciences, Rutgers University, New Brunswick, NJ

[4] NASA Goddard Institute for Space Studies, New York, NY, USA

[5] Center for Climate Systems Research, Columbia University, New York, NY, USA

[6] Potsdam Institute for Climate Impact Research (PIK), Member of the Leibniz Association, Potsdam, Germany

[7] Department of Atmospheric and Oceanic Sciences and Institute of Arctic and Alpine Research, University of Colorado, Boulder, CO, USA

[8] Institut de Ciència i Tecnologia Ambientals (ICTA), Universitat Autònoma de Barcelona, 08913 Cerdanyola del Vallès, Spain

Corresponding author: Charles Bardeen (bardeenc@ucar.edu)

Key Points:

- Global nuclear war injecting 150 Tg of stratospheric smoke causes a peak global ozone loss of 75% with depletion lasting 15 years.

- Ozone loss leads to a tropical UV Index above 35 after 3 years and lasting 4 years, and a 20% global average increase in UV-B, a hazard to life.

- Including smoke decreases photolytic reactions rates, increasing ozone loss by 15% with decreasing NO_x and increasing HO_x catalytic cycles losses.

Abstract

For the first time, we use a modern climate model with interactive chemistry including the effects of aerosols on photolysis rates to simulate the consequences of regional and global scale nuclear wars (injecting 5 and 150 Tg of soot respectively) for the ozone layer and surface ultraviolet (UV) light. For a global nuclear war, heating in the stratosphere, reduced photolysis, and an increase in catalytic loss from the HO_x cycle cause a 15 year-long reduction in the ozone column, with a peak loss of 75% globally and 65% in the tropics. This is larger than predictions from the 1980s, which assumed large injections of nitrogen oxides (NO_x), but did not include the effects of smoke. NO_x from the fireball and the fires provide a small (5%) increase to the global average ozone loss for the first few years. Initially, soot would shield the surface from UV-B, but UV Index values would become extreme: greater than 35 in the tropics for 4 years, and greater than 45 during the summer in the southern polar regions for 3 years. For a regional war, global column ozone would be reduced by 25% with recovery taking 12 years. This is similar to previous simulations, but with a faster recovery time due to a shorter lifetime for soot in our simulations. In-line photolysis provides process specific action spectra enabling future integration with biogeochemistry models and allows output that quantifies the potential health impacts from changes in surface UV for this and other larger aerosol injections.

Plain Language Summary

Nuclear war would result in many immediate fatalities from the blast, heat, and radiation, but smoke from fires started by these weapons could also cause climate change lasting up to 15 years threatening food production. For the first time with a modern climate model, we have simulated the effects on ozone chemistry and surface ultraviolet light caused by absorption of sunlight by smoke from a global nuclear war. This could lead to a loss of most of our protective ozone layer taking a decade to recover and resulting in several years of extremely high ultraviolet light at the surface further endangering human health and food supplies.

1 Introduction

It has been understood since the early days of nuclear weapons testing that nuclear detonations can initiate large-scale fires in urban and rural settings (Glasstone & Dolan, 1977; OTA, 1979; Lewis, 1979). The first estimates of the massive amount of smoke that could be generated in a global-scale nuclear war were made by Crutzen & Birks (1982), and the potential for this amount of smoke injected into the stratosphere to cause global climatic change was shown by the TTAPS study (Turco et al., 1983), where the outcome was likened to a "nuclear winter." Subsequent simulations by scientists in both the United States and the Soviet Union confirmed these results (e.g., Aleksandrov & Stenchikov, 1983; Covey et al., 1984). More recently, these results have been reproduced with modern Earth System models by Robock et al. (2007b) and Coupe et al. (2019) showing climatic effects lasting for over a decade. Prolonged heating and self-lofting by the soot lengthens its lifetime compared to the climatic effects of sulfate from a large volcanic eruption like that of Mount Pinatubo in 1991, which lasted for about 2 years (Robock, 2002).

Originally, it was assumed that a global scale nuclear war between the United States and the Soviet Union would involve weapons with a total yield of 5,000-10,000 Mt with individual weapons having yields up to 20 Mt (Pittock et al., 1986), where a yield of 1 Mt is the energy equivalent of a million tons of TNT. Because of a series of arms control treaties, the inventories of the US and Russia have declined since. Under the New START Treaty, the US and Russia now have a combined total of approximately 6,000 strategic weapons with a total yield of about

72 1,500 Mt and a maximum weapon yield of about 800 kt (Kristensen & Korda, 2020a; Kristensen
73 & Korda, 2020b).
74   In the 1970s, it was realized that the fireball from a nuclear weapon explosion would heat
75 the atmosphere producing nitrogen oxides (NO_x) (Bonner, 1971) and that NO_x in the stratosphere
76 could catalytically destroy ozone (O_3) (Crutzen, 1970). The amount of NO_x produced and the
77 altitude to which it is injected depends on the amount of heating in the fireball, which in turn
78 depends on the yield of the weapon (Foley & Rudderman, 1973). Weapons over about 800 kt
79 would have fireballs energetic enough to directly inject NO_x into the stratosphere (Chang &
80 Wuebbles, 1984). Photochemical simulations including NO_x injections from these large
81 inventories with high-yield weapons showed Northern Hemisphere (NH) O_3 losses varying from
82 about 5 to 60% (e.g. Crutzen & Birks, 1982; Turco et al., 1983, Chang & Wuebbles, 1984,
83 Pittock et al. 1986). In the 1980s, it was realized that smoke from the fires could help loft fireball
84 NO_x into the stratosphere and that heating of the stratosphere by the smoke could affect chemical
85 reaction rates (Turco et al., 1983), but these effects were not included in those early simulations.
86 Kao et al. (1990) demonstrated that heating of the stratosphere added to the NO_x injection would
87 cause a much larger O_3 loss than the NO_x injection alone, but they were only able to run their
88 simulation for 20 days. Recently Mills et al. (2008, 2014) and others (Stenke et al, 2013;
89 Wagman et al. 2020) showed large O_3 loss from a regional nuclear war without including any
90 direct injection of NO_x. The O_3 loss was driven entirely by the heating of the stratosphere by the
91 smoke and the temperature sensitivity of O_3 chemical reactions.
92   O_3 in the stratosphere is a strong absorber of ultraviolet (UV) radiation, which would
93 otherwise be harmful to life at the surface. While sunlight in the UV-C range (200-280 nm) is
94 almost completely absorbed, sunlight in the UV-B (280-300 nm) and UV-A (320-400 nm) ranges
95 does reach the surface. In humans, high levels of UV-B can cause sunburn, photoaging, skin
96 cancer, and cataracts (MacKie, 2000). Photoaging is the premature aging of the skin from
97 exposure to sunlight and can cause pigmentation spots, spider veins, loss of skin tone, and
98 wrinkles. It is also associated with higher skin cancer risks. The World Health Organization uses
99 the UV Index (WHO, 2002) as a metric to inform people about surface UV levels. The scale for
100 UV Index is: low (1-2), moderate (3-5), high (6-7), very high (8-10), and extreme (11+). At the
101 extreme level, unprotected skin can burn within minutes; however, sensitivity does depend on
102 the individual. Some places like the Andes typically have UV Index levels that are considered
103 extreme, but the population is mostly dark-skinned and thus not as sensitive to UV. Because of
104 this a threshold of 16 for extreme has been recommended for this region (Para et al., 2019). At
105 highest risk are people with skin phenotype (SPT) I and II, light skinned people who do not tan
106 easily, residing in areas of high UV as is common in Australia (Molina et al., 2000). Melanomas
107 are the most lethal form of skin cancer representing 4% of cases but half of all deaths, and 60-
108 70% of melanoma cases are thought to be triggered by UV exposure (Sample & He, 2018).
109 Following a regional nuclear war, Mills et al. (2014) found that UV Index increases by 3-6 in the
110 summer at mid-latitudes resulting in UV Index values of 12-21, which are above the existing
111 scales.
112   Recent simulations of the climate effects of a global nuclear war between the US and
113 Russia either did not include interactive chemistry (Robock et al., 2007b) or did not report the O_3
114 loss or surface UV (Coupe et al., 2019). Coupe et al. (2019) did not report their O_3 loss or
115 surface UV because the actinic fluxes used for the photochemistry did not include the attenuation
116 by the smoke. The study in the present paper interactively calculates the actinic flux in the
117 presence of smoke and thus fixes this problem.

118   In this study, we repeat previous simulations of a regional nuclear war between India and
119 Pakistan producing 5 Tg of soot (Robock et al., 2007a; Mills et al. 2008, 2014; Stenke et al.,
120 2013; Toon et al., 2019, Wagman et al., 2020) and a global nuclear war between the US and
121 Russia producing 150 Tg of soot (Robock et al., 2007b; Coupe et al., 2019). Our simulations are
122 focused on the changes to O_3 and surface UV using an Earth System model with interactive
123 chemistry and a sophisticated treatment of soot particles that includes the effects of aerosols on
124 photolysis. We include a series of sensitivity tests with varying amounts of NO_x injection, both
125 with and without including aerosols in the calculation of actinic flux, to better characterize the
126 importance of smoke, NO_x and these processes on determining the effects of nuclear war on
127 ozone.
128   Both of these cases were originally defined based upon older weapons inventories. The
129 weapons inventories held by India and Pakistan have likely increased in both quantity and yield,
130 making the 5 Tg estimate on the conservative side of what might actually occur (Toon et al.,
131 2019). The US and Russia have decreased the number and size of their weapons, so the 150 Tg
132 estimate is likely an overestimate for a counterforce war with targets in just those two countries,
133 but Toon et al. (2008) estimated 180 Tg or more was possible if these countries included targets
134 in Europe and Asia. The exact amount of soot injected depends on details of the weapons used
135 and the specific targets, so it is highly uncertain and an area of active research. Using these
136 previously defined cases allows us to explore the range of possible values and to more easily
137 compare with prior results.
138   We compare the resulting O_3 losses to those found in prior studies, perform sensitivity
139 tests for including aerosols in photolysis and various NO emissions, and discuss the implications
140 of the O_3 and UV changes on the biota. For the first time, these simulations have an in-line
141 calculation for the actinic flux that includes aerosols, which provides improved photolysis rates,
142 and high spectral resolution fluxes allowing the output of spectral action functions, weighted
143 integrals over specific wavelength ranges, for biologically important processes. Section 2
144 describes the model setup, Section 3 presents the results and discusses UV impacts, and Section
145 4 discusses the implications of these results.

146 **2 Methods**

147 2.1 WACCM4 Model

148 We use the Community Earth System Model (CESM) (Hurrell et al., 2013), a chemistry climate
149 model with interactive atmosphere, land, ocean, and sea ice. The ocean model simulates the
150 evolution of physical and biogeochemical parameters at 1˚ horizontal resolution with 60 vertical
151 layers of varying depth by coupling the Parallel Ocean Program (POP) version 2 ocean physical
152 model (Danabasoglu et al., 2012) with the Biogeochemical Elemental Cycling ocean
153 biogeochemical model (Lindsay et al., 2014). The land model is the Community Land Model
154 (CLM) version 4 with a carbon-nitrogen cycle and simulates the evolution of the land physical
155 state, characteristics of the land surface, exchanges of energy and material with the atmosphere,
156 and run-off into the ocean. It has a horizontal resolution of 1.9˚x2.5˚ with 15 vertical layers for
157 the land and 10 vertical layers for lakes. (Oleson et al., 2010; Bonan et al., 2011).
158   The atmospheric model is the Whole Atmosphere Community Climate Model version 4
159 (WACCM4) (Marsh et al., 2013) which has a model top around 140 km, a horizontal resolution
160 of 1.9˚x2.5˚, 66 vertical levels, and includes interactive chemistry. The chemistry mechanism
161 used in this study includes a detailed representation of the middle atmosphere, with a
162 sophisticated suite of gas-phase and heterogeneous chemistry reactions including the odd-oxygen

163   (O_x), odd-nitrogen (NO_x), odd-hydrogen (HO_x), odd-chlorine (ClO_x), and odd-bromine (BrO_x)
164   reaction families. WACCM4 has been used successfully in numerous studies of stratospheric O_3
165   chemistry (e.g., Solomon et al., 2015; Solomon et al., 2016; Polvani et al., 2017; Randel et al.,
166   2017; Stone et al., 2019; Froidevaux et al., 2019). Vertical resolution in WACCM4 is about 1.25
167   km in the troposphere and stratosphere and 2.5 km in the mesosphere. To stabilize the model
168   against the large soot perturbations, the changes described in Bardeen et al. (2017), including the
169   addition of the Rapid Radiative Transfer Model for GCMs (RRTMG) (Iacono et al., 2000), are
170   used for all these simulations.
171   All simulations are free running and external forcings, other than soot and NO_x, are
172   configured for repeated year 2000 conditions. A control simulation was run for 19 years and each
173   war simulation starts at year 4 of the control and lasts for 15 years allowing most simulations to
174   return to steady state.

175   ## 2.2 War Scenarios
176   In this study, two types of wars are simulated: a regional nuclear war between India and
177   Pakistan, and a global nuclear war between the United States and Russia. The regional war
178   follows the 5 Tg of soot scenario described in Toon et al. (2019) using 44 15 kt-weapons with
179   urban targets in a war lasting 3 days and is similar to that used by Mills et al. (2008, 2014).
180   Smoke is emitted instantaneously when a target is attacked. The global war follows Coupe et al.
181   (2019) and is similar to that used by Robock et al. (2007b). It assumes that 150 Tg of soot is
182   emitted uniformly over the continental US and Russia. The war lasts 7 days and the smoke
183   emissions ramp down linearly during that time. As was done in previous studies, these wars are
184   assumed to start on May 15th of the first year. Coupe et al. (2019) and Robock et al. (2007b) did
185   not include weapon counts or yields needed for determining NO_x emissions, so we have
186   performed sensitivity tests with weapons inventories from: Toon et al. (2008), Kristensen &
187   Korda (2020a, 2020b), and NRC (1985).

188   ## 2.3 Soot Treatment and Emissions
189   Soot aerosol is treated using the Community Aerosol and Radiation Model for Atmospheres
190   (CARMA) (Toon et al., 1988; Bardeen et al., 2006), a sectional microphysics model that allows
191   aerosols and the processes that affect them, including coagulation and sedimentation, to be
192   treated in a size-resolved manner. The CARMA treatment for soot follows Bardeen et al. (2017)
193   and has been used in previous studies of smoke from nuclear war (Coupe et al., 2019; Toon et
194   al., 2019). Rather than treating the soot as one large spherical particle of pure black carbon (BC),
195   as is often done in aerosol models, we treat the soot as fractal particles, clusters of smaller
196   spheres of a uniform size (monomers) whose spatial arrangement is described by its fractal
197   properties. We assume a monomer radius of 30 nm, a fractal dimension of 2.2 and a packing
198   coefficient of 1, which creates a particle whose overall shape is more like a sheet than a sphere.
199   This affects the fall velocity, coagulation rate, and optical properties of the soot. The particles are
200   emitted in a log-normal size distribution with a mean of the radius of a sphere with equivalent
201   mass of 0.11 μm and a width of 1.6. All soot is emitted in the vertical as a constant mixing ratio
202   between 150 and 300 hPa.

203   ## 2.4 NOx Emissions
204   NO_x is a shorthand for the combination of nitric oxide (NO) and nitrogen dioxide (NO_2). It can
205   be created by the heat from the fireball of the nuclear explosion as well as being emitted from the
206   surface fires cause by the explosion. NO_x in the model is emitted only as NO. There is a rapid
207   cycling between NO and NO_2 driven by NO_2 photolysis during the day and rapid reformation of

208 NO₂ at night, so the choice of the NO_x species to use for emissions is not important (Brasseur &
209 Solomon, 2005).

210 ### 2.4.1 Fireball NO_x
211 The amount of NO created in the fireball is proportional to the yield of the weapon. These
212 simulations assume a rate of 1×10^{32} molecules of NO injected per Mt of yield (NAS, 1985). The
213 emissions are spread uniformly between the top and bottom of the fireball. The fireball height is
214 a function of yield determined using equations adapted from Chang et al. (1979) that fit results
215 from Foley & Rudderman (1973):

$$Z_{top} = 21.64 Y^{0.2} + \left(Z_{trop} - Z_{ref} \right) \qquad (1)$$

$$Z_{bot} = 13.41 Y^{0.2} + \left(Z_{trop} - Z_{ref} \right) \qquad (2)$$

218 where Z_{trop} is the tropopause height at the target (km), Y is the yield of the weapon (Mt), Z_{ref} is a
219 reference height of the tropopause (17 km), and Z_{top} (km) and Z_{bot} (km) are the heights of the top
220 and bottom of the fireball. These equations have been adapted to account for the local tropopause
221 height as the data from Foley & Rudderman (1973) were based upon atmospheric tests that were
222 at low to mid-latitudes while a nuclear war between the US and Russia would occur mostly at
223 mid- to high latitudes where the tropopause is lower. Fireball NO is emitted at the time of the
224 weapon detonation. For the regional case the weapon use is spread out over 3 days (Toon et al.,
225 2019), but for the global war case all the NO is released at the start of the war. Since we do not
226 here have a detailed war plan for the global war case indicating when the weapons would be
227 used, we have assumed that all the weapons are used and thus all the fireball NO is released on
228 the first day.

229 ### 2.4.2 Fire NO_x
230 NO can be emitted from fires as part of the combustion process. Wildfire data from Andreae
231 (2019) are used to estimate that ~2 g of NO is emitted per kg of fuel burned. Using the
232 assumption of 20 g of black carbon (BC) per kg of fuel (Toon et al., 2007) that was made to
233 determine the soot emissions for the war scenarios, gives us a ratio of 0.1 g NO per g BC. NO is
234 assumed to be emitted at the same location and with the same timing as the soot emissions.

235 ### 2.5 In-line Photolysis
236 In WACCM4, photolysis was previously calculated by first using a lookup table (LUT) to
237 calculate the actinic flux in 100 wavelength bands between 121 and 750 nm and then by applying
238 the cross-section and quantum yield for each photolysis reaction adjusted for the local
239 temperature and pressure (Kinnison et al., 2007). Thus the cross-sections and quantum yields
240 were affected by heating caused by solar absorption from aerosols, but photolysis rates did not
241 include the direct effects on actinic flux from aerosol scattering and absorption. This approach
242 was used by Mills et al. (2008, 2014), Toon et al. (2019), and Coupe et al. (2019). For this study
243 we added the Tropospheric Ultraviolet and Visible (TUV) model (Madronich & Flocke, 1997)
244 version 4.2 to provide an in-line calculation of the actinic flux.
245   The older calculation of the photolysis coefficients is divided into two regions: (1) 120
246 nm to 200 nm (33 wavelength intervals); and (2) 200 nm to 750 nm (67 wavelength intervals).
247 The total photolytic rate constant for each absorbing species was derived during model execution
248 by integrating the product of the wavelength dependent top of the atmosphere flux; the
249 atmospheric transmission function (or normalized actinic flux), the molecular absorption cross-
250 section, and the quantum yield. The top of the atmosphere flux over these wavelength intervals
251 can be specified from observations and varied over the 11-year solar sunspot cycle. The
252 wavelength-dependent transmission function was derived as a function of the model abundance

253 of O_3 and molecular oxygen. For wavelengths beyond 200 nm a flux LUT approach was used,
254 based on the 4-stream off-line version of TUV. The transmission function was interpolated from
255 the LUT as a function of altitude, column O_3, surface albedo, and zenith angle. The LUT
256 assumed a mid-latitude O_3 profile and scaled the result based upon the total column O_3. This
257 older approach did not include the effects of aerosols or sulfur dioxide (SO_2).
258   The temperature and pressure dependences of the molecular cross sections and quantum
259 yields for each photolytic process were also represented by another LUT in these wavelength
260 regions. At wavelengths less than 200 nm, the wavelength-dependent cross section and quantum
261 yields for each species are specified and the transmission function is calculated explicitly for
262 each wavelength interval. There are two exceptions to this approach. In the case of the
263 photolysis rates for NO and molecular oxygen (O_2), detailed photolysis parameterizations are
264 included in-line. In the Schumann-Runge band region, the parameterization of NO photolysis in
265 the δ-bands is based on Minschwaner & Siskind (1993). This parameterization includes the
266 effect of self-absorption and subsequent attenuation of atmospheric transmission by the model-
267 derived NO concentration. For O_2 photolysis, the Schumann-Runge band and Lyman-alpha
268 parameterizations are based on Koppers & Murtagh (1996) and Chabrillat & Kockarts (1997,
269 1998), respectively.
270   For the current study we added the TUV model to provide an in-line calculation of the
271 actinic flux. The in-line version differs from the LUT approach discussed above in that a 2-
272 stream version of TUV was used for computational efficiency. For consistency with prior work,
273 the same band structure, cross-sections, and quantum yields are used. Using in-line TUV allows
274 the actual O_3, SO_2, and aerosol profiles in the column to be included in the calculation. For the
275 aerosols, the optical properties calculated for the coarser band structure used by the radiative
276 transfer code have been interpolated onto the wavelength grid used by TUV. TUV is also able to
277 output spectral integrals of useful radiative fluxes and biologically important action spectra such
278 as UV-B and photosynthetically available radiation (PAR, 400-700 nm) that can aid in
279 understanding the effects on the biota of the changes to O_3 and to the aerosols.

280 ## 3 Results and Discussion

281 We first describe changes to O_3 and surface UV from a regional nuclear war compared to results
282 from Mills et al. (2008, 2014) and then evaluate O_3 depletion following a global nuclear war
283 compared to results from the 1980s (Pittlock et. al, 1986; Kao et al., 1990). All the WACCM4
284 simulations made for this study are summarized in Table 1. The notation has the name of the
285 potential conflict (e.g., IP is India-Pakistan) and the base cases include TUV with aerosols
286 affecting photolysis and NO emission from the fireball and the fires. A minus sign (–) indicates
287 that a process is not included (e.g., IP–AOD means the India-Pakistan case, but not accounting
288 for the effects of aerosols, using AOD to mean aerosol optical depth, in the chemistry
289 calculations) and a plus sign (+) indicates that alternate fireball NO emissions were used.
290 Climate effects other than those related to O_3 and surface UV have already been described in
291 Coupe et al. (2019) for the global war case and Toon et al. (2019) for several regional war cases.
292 Our climate results are similar to these and thus will not be discussed here; however, we do show
293 the evolution of the global (Figs. 1, S1) and polar (Figs. S2, S3) average vertical profile changes
294 for soot, temperature, H_2O, HO_x, NO_x, and O_3 from our regional and global war cases.

295 ### 3.1 Regional Nuclear War

296 Mills et al. (2008, 2014) assumed that a nuclear conflict involving India and Pakistan generated 5
297 Tg of soot with the soot spread uniformly over the region. Mills et al. (2008) used WACCM3
298 and Mills et al. (2014) used WACCM4 with a fixed size of 100 nm for the soot to simulate the

299   resulting climate effects. Toon et al. (2019) recreated a similar case; however, they used
300   emissions from a specific set of targets and weapon yields, a fractal representation for the soot,
301   and the soot was allowed to coagulate. This study repeats Toon et al. (2019) but includes in-line
302   photolysis from TUV as well as NO_x emissions from the fireballs and the fires. Figure 2 shows
303   the evolution of the change in the monthly global average O_3 column for several cases compared
304   to their control cases. All these cases show a peak O_3 loss of ~25% 2-3 years after the war, but
305   the fractal soot cases (IP, IP–NO, IP–AOD, and Toon et al., (2019)) all show a faster recovery of
306   12 years than Mills et al. (2008, 2014), because the soot particles grow larger (> 500 nm) and
307   thus have a shorter lifetime in the stratosphere. Mills et al. (2008) showed faster O_3 recovery than
308   that in Mills et al. (2014) because Mills et al. (2008) used specified sea surface temperatures and
309   had a horizontal resolution of 4° latitude by 5° longitude, which led to a faster stratospheric
310   circulation and shorter soot lifetime than Mills et al. (2014), which has an interactive ocean and a
311   horizontal resolution of 1.9° latitude by 2.5° longitude (Mills et. al, 2014). Including NO
312   emissions (IP versus IP–NO) does slightly increase O_3 loss, mostly by slowing the recovery, but
313   the effects are minor because the amount of NO injected is small and the temperature effects are
314   so strong. Including aerosols in the photolysis calculations (IP versus IP–AOD) slightly
315   decreases the amount of O_3 loss, but the effect is not significant.
316   Mills et al. (2008, 2014) did not include NO_x emissions and found that O_3 loss was
317   primarily driven by heating of the stratosphere and temperature dependencies in ozone
318   decomposition and NO_x catalytic losses along with additional N_2O transport and longer NO_x
319   lifetimes. Figure 3 shows the global average total column odd-oxygen chemical reaction rates for
320   the IP (Fig. 3b), IP–AOD (Fig. 3a), and IP-NO (Fig. 3c) cases as solid lines. The individual
321   chemical reactions that are important to odd-oxygen chemistry and their contribution to these
322   subtotals (Brasseur & Solomon, 2005) are shown in Table 2. Mills et al. (2008) did not output all
323   of these individual rates, but their results should be similar to the IP–AOD case. Both cases show
324   an increase in O production, which is primarily because of a temperature sensitivity in the
325   photolysis cross section for the $O_2 + h\nu \rightarrow 2O$ reaction. The IP case has lower overall reaction
326   rates, because photolysis is reduced compared to the IP–AOD case by the reduced actinic flux
327   caused by solar absorption from the soot. However, the total production and loss rates are greater
328   than the control, indicating that the temperature effects are greater than the effects caused by the
329   reduced actinic flux. There is a small increase in NO_x loss in the IP case compared to the IP-NO
330   case, but the effects of the NO injection are negligible.
331   Looking at these rates relative to the total production of odd-oxygen (Figure 4) shows
332   that HO_x, ClO_x, and BrO_x catalytic cycles decrease relative to the control while the NO_x catalytic
333   cycle and O_3 decomposition (O_x) increase. The magnitude of these changes is less when the
334   aerosols are included in the photolysis calculation. Though HO_x remains the dominant odd-
335   oxygen loss mechanism, as reported by Mills et al. (2008), increases in NO_x and O_x are the
336   drivers of increased O_3 loss following a nuclear conflict. The absolute contribution from HO_x
337   stays fairly constant leading to a decreased relative contribution as odd-oxygen production
338   increases. We also see both an absolute and relative decrease in the ClO_x and BrO_x catalytic
339   cycles that was not seen by Mills et al. (2008). The O_x, ClO_x, and BrO_x changes last about 2
340   years while NO_x changes last about 6 years. HO_x changes switch from relative decrease for 6
341   years to a slight relative increase for another 4 years.
342   Figure 5 shows the vertical profile of the global average chemical rates and O_3 profile for
343   the first year after the war for the IP–AOD and IP cases and the corresponding change in
344   temperature is shown in Figure S4. The O_3 profiles are similar for the IP–AOD and IP cases with

345 reductions in the stratosphere and upper mesosphere. The IP–AOD case shows about a 20%
346 increase in O production relative to the control in the stratosphere, but the IP case shows little
347 change in O production relative to the control case when aerosols affect the actinic flux.
348 Similarly, there is a large increase relative to the control in odd-oxygen loss from NO_x and O_x in
349 the IP–AOD case in the stratosphere that is smaller in the IP case. In both cases, HO_x driven loss
350 is increased in the stratosphere relative to the control, but reduced in the lower mesosphere and is
351 nearly identical to the control in the troposphere and upper mesosphere contributing to the small
352 change in HO_x loss rates seen in the total column (Figure 3).
353   Figure 6a shows the evolution of the change in zonal average column O_3 for the IP case,
354 while absolute amounts are shown in Figure S5b. Similar to Mills et al. (2014), we see a greater
355 percentage loss, up to 60%, at higher latitudes and losses on the order of 10% in the equatorial
356 tropics. As seen in the global average (Fig. 2), the O_3 recovers faster in our simulation than in
357 Mills et al. (2014) because the soot particles get larger and have a shorter lifetime.
358   These O_3 changes cause an increase in the surface UV Index (Fig. 7b). The values shown
359 are the monthly average of the daily maximum clear-sky values calculated by TUV. The daily
360 maximum value should be close to the noon local time value that is commonly reported for UV
361 Index; however, observed values at exactly noon local time or averaged over 30 minutes around
362 noon local time may be lower than the maximum daily value by several points (Para et al., 2019).
363 Compared to the control run (Figs. 7a, S6a), there is an increased surface UV immediately
364 following the war lasting for about 6 years. Since surface UV is a function of the Sun, aerosols,
365 clouds, and O_3, the areas of the largest O_3 depletion do not necessarily show the largest increases
366 in surface UV. Values of 20 or larger are found between 30˚S to 20˚N the control case, but
367 extend to 40˚S to 40˚N in the IP case. The largest increases in the IP case occur in the southern
368 polar region around 70˚S, which is far removed from where the smoke was injected. The
369 consequences of these changes in surface UV on the biota will be discussed in section 3.3.

370 3.2 Global Nuclear War
371 Coupe et al. (2019) used WACCM4 to simulate the effects of a nuclear war between the United
372 States and Russia using a scenario similar to Robock et al. (2007b), but with the same soot
373 representation used in Toon et al. (2019). This study repeats Coupe et al. (2019) but includes in-
374 line photolysis from TUV and NO_x emissions from the fireballs and the fires. Figure 8 shows the
375 evolution of the change in column O_3 for the NH (Fig. 8a) and globally (Fig. 8b). Connell &
376 Wuebbles (shown in Pittock et al., 1986) used a photochemical model to assess O_3 changes from
377 3 different weapons inventories from AMIBIO (1982), Knox (1983), and NRC (1985) but only
378 included effects from the fireball NO_x with no heating caused by the soot. The largest reduction
379 they found was about 45% using the Knox (1983) inventory and the losses lasted about 10 years.
380 Kao et al. (1990) included the effects of the soot and the fireball NO_x, but only in a short
381 simulation that lasted 20 days. They used the NRC (1985) inventory, but achieved much larger
382 loss of 15% in 20 days than Connell & Wuebbles did with the same inventory.
383   Coupe et al. (2019) showed that the stratospheric heating in the global war case is
384 stronger than for a regional war and we show this heating results in O_3 losses of up to 80% in the
385 NH with losses lasting for 15 years. The difference in O_3 loss between our extreme cases for NO_x
386 emissions (UR–NO and UR+NO3) is up to 15% in the NH and 10% globally. Removing the
387 aerosols from the actinic flux calculation (UR–AOD) results in less O_3 loss by over 20% in the
388 NH and 15% globally. The cause for this lower loss of O_3 can be seen in the global average
389 chemical reaction rates (Fig. 9). The heating alone causes an almost 3 times increase in reaction
390 rates (Fig. 9a); however, when the aerosols are included in the actinic flux (Fig. 9b), the reaction

9

391 rates drop to less than a quarter of the unperturbed rates and more than compensate for the
392 heating induced increase. Thus unlike the IP case, the reduction in actinic flux has a bigger
393 impact on O_3 than the temperature changes in the UR case as the total production and loss are
394 much lower than seen in the control. Including the NO injection (Fig. 9c) causes a small increase
395 in the NO_x loss for the first few years. The UR–AOD (Fig. 10a) and UR (Fig. 10b) cases show
396 very different relative reaction rates. UR–AOD suggests that the HO_x cycle decreases initially
397 and that the NO_x cycle and O_x decomposition drive the O_3 loss, similar to what was seen in the
398 IP case. However, in the UR case, the HO_x cycle actually increases for 15 years, while the NO_x
399 cycle increases for 6 years and then decreases for 9. O_x decomposition decreases slightly and
400 ClO_x and BrO_x cycles decrease for 10 years. O_3 production in the troposphere takes on a more
401 important role as O production is greatly diminished.
402   The global average vertical profile for the first year also shows significant differences
403 between the UR–AOD (Fig. 11a) and UR (Fig. 11b) cases. In the UR case, all reaction rates in
404 the stratosphere are significantly reduced compared to UR–AOD. Both simulations show a
405 greatly reduced stratospheric O_3 layer, with UR having a larger peak in the mesosphere than UR–
406 AOD, where O production by photolysis is largely unaffected.
407   Figure 6b shows the evolution of the zonal average change in the O_3 column for the UR
408 case, while absolute amounts are in Figure S5c. Losses at mid to high latitude exceed 75% and
409 over 65% in the tropics during the first few years. Recovery in the tropics is faster than at high
410 latitude, but still takes 10 years to recover to within 5% of the control case. Initially, the soot
411 compensates for the O_3 loss and UV is actually reduced at the surface (Figs. 7c, S6b) compared
412 to the control (Fig. 7a). However, the UV Index begins to increase relative to the control after 3
413 years as the soot clears reaching a peak 8 to 9 years after the war. UV Index values of 35 are seen
414 in the tropics from years 5 to 8, and are greater than 45 during the summer in the southern polar
415 regions from years 5 to 8. Maps of UV Index for selected months averaged over years 8 to 10
416 show a generally zonal structure but with regions of extreme UV including higher altitudes and
417 deserts (Fig. S8).
418 3.3 Effects of Surface UV Changes
419 Soot injected into the atmosphere absorbs sunlight heating the stratosphere and reducing the
420 solar radiation at the surface causing lower surface temperatures and reduced precipitation. The
421 heating in the stratosphere causes increased O_3 destruction that allows more UV radiation to the
422 surface. Effects from these climatic changes for regional wars have been discussed in Robock et
423 al. (2007a), Stenke et al. (2013), Mills et al. (2014), and Toon et al. (2019). Jägermeyr et al.
424 (2020) found large agricultural changes and Scherrer et al. (2020) predicted significant effects on
425 fisheries in response to climatic changes from a regional nuclear war. Scherrer et al. (2020) also
426 found larger effects for the global war case. However, neither study included the effects of O_3 or
427 UV changes, which would likely lead to additional losses especially related to global grain
428 productivity. The effects of a global nuclear war were studied in the 1980s (e.g., Crutzen & Birks
429 (1982), Turco et al. (1983), Harwell et al. (1986)), but these studies did not include the effects of
430 stratospheric heating on O_3 loss. Robock et al. (2007) and Coupe et al. (2019) revisited these
431 global war studies, but did not include estimates of changes to stratospheric O_3 or surface UV.
432   Figure 12 shows the evolution of global average aerosol optical depth (AOD), surface
433 temperature, precipitation, O_3, PAR, UV-A, and UV-B for the IP and UR cases. In both cases,
434 PAR and UV-A is reduced by the presence of the aerosol, but UV-B responds differently in the
435 two cases. The major absorber for UV-B is O_3, so in the IP case (Fig. 12a), which added a
436 smaller amount of soot but still has significantly lowered O_3, UV-B increases by up to 10% in

437   proportion to the O_3 destruction. For the UR case (Fig. 12b), so much soot is injected that even
438   though the O_3 loss is greater than in the IP case, there is still a dramatic reduction in UV-B, UV-
439   A, and PAR. However, in the UR case, the soot is removed faster than the O_3 recovery, so after 7
440   years there is a net 20% increase in UV-B. UV-B remains elevated for 8 more years, while PAR
441   recovers after 10 years. Photosynthetic organisms in terrestrial and marine environments are
442   sensitive to the ratios of UV-B, UV-A, and PAR (Krizek, 2004). High levels of UV-B can
443   contribute to inhibition of photolysis affecting photosystem II (Hakala-Yatkin et al., 2010, Ragni
444   et al., 2008, Kataria et al., 2014) reducing leaf expansion (e.g. Searles et al., 2001) and plant
445   growth rate (Allen et al. 1998; Ballaré et al. 2001; Ballaré et al. 2011). However, some UV-B
446   damage may be offset by supplemental PAR and UV-A radiation involved in the repair process
447   (Krizek, 2004) with plants adapting to higher UV-B by producing compounds such as plant
448   pigmentation which might improve the quality of certain crops (Bassman, 2004; Bornman et al.,
449   2015). Unfortunately, in our nuclear war scenarios we see increased UV-B along with decreased
450   UV-A and PAR, suggesting photosystem II damage and a simultaneous slowing of repair
451   processes. In the IP case, PAR, UV-A, and UV-B return to within a few percent of normal levels
452   at the same time; however, in the UR case UV-A and PAR return to within a few percent of
453   normal levels 5 years before UV-B which may offset some of the potential damage.
454   UV can have both beneficial and harmful effects on humans. UV-B is needed for vitamin
455   D synthesis and UV-A helps prevent seasonal affective disorder, a type of depression associated
456   with the change of seasons (MacKie, 2000). Vitamin D deficiency can lead to rickets, a disease
457   that can cause weak or soft bones in children and a similar disease called osteomalacia in the
458   elderly. Because of this, vitamin D is often added as a food supplement, for example, to milk.
459   Vitamin D deficiency has also been linked to chronic diseases like cardiovascular disease and
460   cancer, and it is especially prevalent in minority groups, likely due to a combination of genetic
461   (pigmentation) and socioeconomic factors (Forrest and Struhldreher, 2011). On the other hand,
462   there are several serious harmful effects of increased UV-B including sunburn, photoaging, skin
463   cancer, and cataracts (MacKie, 2000). People with either a genetic or drug-induced sensitivity to
464   UV or who are genetically unable to repair DNA damage may be particularly affected. UV-C
465   (200-280 nm) is readily absorbed by O_3 and thus does not reach the surface and is generally not
466   considered in terms of effects on human health (MacKie, 2000).
467   To better understand the role of UV radiation on biota, various action spectra have been
468   identified that integrate a portion of the spectrum that is important for particular biological
469   processes. Figure 13 shows examples of changes in the action spectra calculated by TUV for
470   plant growth (Flint, 2003), phytoplankton inhibition (Boucher, 1994), vitamin-D synthesis
471   (Bouillon et al., 2006), cataract formation (Oriowo, 2001), solar induced erythema (Anders,
472   1995), and DNA damage (Setlow, 1974) along with the UV-B spectrum for the IP and UR cases.
473   The changes in the action spectra generally follow the shape of UV-B, but the magnitudes may
474   be different. For the IP case (Fig. 13a) these are generally positive for 10 years following the
475   war. Plant growth, which refers to the height of light-grown oat seedlings, is the only one that
476   experiences a negative change which persists for 2 years. The largest increase of up to 40% is for
477   DNA damage, a proxy for forming human skin cancers. The next largest is erythema (sunburn)
478   which increases at up to 28% closely followed by vitamin-D synthesis. Cataract damage, the
479   formation of cloudy spots on pig eye lenses, closely matches the changes in UV-B, with up to a
480   19% increase. Finally, UV inhibition of phytoplankton carbon absorption, increases by up to
481   11%. The UR case (Fig. 13b) shows the same general relationship between the magnitudes of the
482   different action spectra. However, each action spectra first experiences negative changes with a

483   90% reduction and then becomes positive after a period of time. Vitamin-D synthesis is negative
484   for the first 4 years, indicating a brief period of extreme risk for rickets. The DNA damage
485   metric becomes positive within a year and reaches a peak increase of 140%. The others show
486   positive values after 4 to 7 years, with peak increases between 10 and 60%.
487   UV that could cause DNA damage increases rapidly in the UR case because of the shapes
488   of the O_3 and soot absorption spectra. Figure 14a shows the O_3 absorption cross-section
489   (Gorshelev et al., 2014) and the soot mass absorption coefficient for 0.16 μm particles in the
490   range of 230 to 370 nm, both normalized by the maximum value within that range. O_3 has a very
491   strong peak around 255 nm, but does absorb across this entire wavelength range. Soot absorption
492   decreases by 40% from 230 to 370 nm. Figure 14 shows the evolution of changes in UV-B and
493   action spectra related to human skin cancer: erythema, DNA damage, and skin cancer (de Gruijl
494   & Van der Leun, 1994; CIE 2006) for the IP and UR cases. In the control (not shown) O_3
495   absorbs essentially all of the UV-C and a large fraction of the UV-B light. In the IP case (Fig.
496   14b), the moderate loss of O_3 causes an increase in surface UV. In the UR case (Fig. 14c), even
497   though there is a much larger loss of O_3, there is a decrease in surface UV-B because of the large
498   UV absorption by the soot. As the soot is removed, the surface UV increases gradually over 8
499   years. UV-B is larger compared to the control starting 4 to 7 years after the war, depending on
500   the exact spectral weights of the action function. However, lost O_3 absorption in the UV-C range,
501   that could cause DNA damage and where O_3 is most absorbing, is not compensated for by the
502   increased but relatively weaker soot absorption. This leads to the rapid and large increase of
503   DNA damaging UV in the UR case; however, this increase is from very low levels, so UV-C is
504   still probably not a health threat for either nuclear war case. UV-C changes may need to be
505   accounted for when O_3 loss is larger, for example following fires generated by an asteroid impact
506   at the K-Pg boundary (Bardeen et al., 2017).
507   While CESM is capable of simulating the ocean physical, biogeochemical, and ecological
508   response to nuclear war (e.g., Lovenduski et al., 2020; Scherrer et al. 2020; Coupe et al., 2021),
509   the version of CESM used in this study does not include the effect of UV inhibition on
510   phytoplankton growth, which may affect each taxa differently (Jeffrey et al., 1999; Xu et al.,
511   2016; De Tommasi et al., 2018). Diatoms, which are the dominant phytoplankton functional type
512   outside the oligotrophic subtropical gyres, have a silica shell that may provide UV protection,
513   while in the gyres small phytoplankton dominate, which with the exception of coccolithophores
514   have no known UV protection. Future work will address this issue by including a representation
515   of UV inhibition in lower trophic levels. Changes in phytoplankton will in turn influence their
516   consumers, i.e. fish and other higher trophic-level organisms (Stock et al., 2017). In this way, the
517   war-driven changes in UV might have bottom-up effects on fish and fisheries that could be
518   estimated in future work. Experiments indicate that many shallow-living marine organisms and
519   freshwater fish are directly harmed by increasing levels of UV-A and UV-B (Llabrés et al., 2013;
520   Alves & Agustí, 2020). However, the direct effects of UV on the fish in the wild are poorly
521   known, leaving the impact of UV changes on fish and fisheries highly uncertain.
522   UV effects on plant growth are complex and currently not represented in most crop and
523   land surface models (Wargent and Jordan, 2013), but recent model development is trying to
524   address and quantify related processes. Surface O_3 also changes in these simulations (Fig. S7)
525   and can have severe impacts on plant growth and crop yields by decreasing plant photosynthesis
526   rates and stomatal conductance (Lombardozzi et al., 2012; Lombardozzi et al., 2013). Surface O_3
527   is strongly affected by the Stratosphere-Troposphere-Exchange (STE) and tropospheric
528   photochemistry (Xia et al., 2017). While these simulations do show a significant change in

529   surface O_3 from STE, they do not include detailed tropospheric chemistry and thus cannot fully
530   assess the changes to surface O_3. Impacts of surface O_3 on plants and crop yields are not
531   currently simulated by Earth System models or most process-based crop models (Schauberger et
532   al. 2019); however, there are an increasing number of pilot studies including an O_3 damage
533   function in land models (Lombardozzi et al., 2015) and crop models (Emberson et al. 2018).
534   CESM does not have a built-in capability to track effects upon human health, but the
535   availability of these action spectra could enable additional capabilities in the future. Humans if
536   properly informed and equipped have the ability to adapt to these changes by staying indoors,
537   only going out at night, or by covering up with clothes and sunscreens. Plants and animals are
538   also sensitive to these changes. While ranchers may be able to make adaptations for livestock,
539   wild populations of plants and animals will be exposed to the direct effects of these UV changes.

540   **4 Conclusions**

541   In this study, we conducted simulations of regional and global scale nuclear war impacts on
542   ozone using a modified version of WACCM4 that for the first time includes in-line calculations
543   of actinic flux using TUV. This allows for the inclusion of aerosols in the photolysis calculation
544   and for the diagnostic output of action spectra that can help quantify ecosystem and health
545   effects. We also included the emissions of NO from the fireball and the surface fires. For
546   regional wars, we find that while including aerosols in the photolysis calculation does change
547   reactions rates, the effects of this and NO emissions does not make a significant change in the O_3
548   loss relative to earlier calculations that did not include them. This results in a peak global
549   average loss of ~25% with much larger losses of up to 55% at high latitudes. We find that the
550   HO_x catalytic cycle remains the largest loss mechanism, but is largely unchanged as found by
551   Mills et al. (2008). Also, as reported by Mills et al. (2008), the increase in the NO_x cycle and O_x
552   decomposition drive the increased O_3 loss. We see a reduction in loss from the ClO_x and BrO_x
553   cycles that was not reported previously.
554   For global nuclear war, we provide the first estimates of O_3 and surface UV from modern
555   climate models and find much greater O_3 loss than was predicted in the 1980s, with a peak global
556   average loss of 75%. While the weapon sizes and therefore NO emissions have decreased since
557   the 1980s, the inclusion of smoke and the heating of the stratosphere causes significant O_3 loss as
558   demonstrated by Kao et al. (1990) and shown for regional wars by Mills et al. (2008). For the
559   global war, the inclusion of aerosols in the photolysis calculations show large changes in
560   chemical reaction rates and 15% larger peak O_3 loss. We also show that reduced O production
561   and the HO_x cycle dominate the increased O_3 loss with a contribution from the NO_x cycle for the
562   first few years.
563   The warming of the higher polar latitudes (Figs. S2, S3, S4) in both the IP and UR cases
564   greatly reduces the importance of the standard chlorine and bromine heterogeneous chemistry for
565   O_3 depletion. For the UR case, the zonal winds are significantly altered compared to the control
566   and the overall stratospheric Brewer Dobson circulation changes affect the transport of odd-
567   oxygen loss precursors into the polar lower stratosphere. Poleward and downward transport of
568   NO_x is increased by more than 150% in the IP case and more than 400% in the UR case relative
569   to the control. Increased stratospheric H_2O from a warmer tropopause increases H_2O in the SH
570   polar region to values greater than 8 ppmv and 150 ppmv relative to the control in the IP and UR
571   cases respectively. Consequently HO_x is also increased by over 100% and 500% in these two
572   cases (Fig. S2). Air depleted of O_3 is also transported from the upper/middle stratosphere into the
573   lower polar stratosphere. Depletion of total column ozone (TCO) is much greater for the six

574 years after the IP event than in the control (Figs. 6, S5). This depletion is not limited to just the
575 September and October periods, but throughout the SH polar season due to increases in NO_x and
576 HO_x. The IP event would cause a short-term hiatus in the recovery of TCO (e.g., Solomon et al.,
577 2016) of approximately 10 years. TCO depletion from the UR case in the SH polar latitudes is
578 extreme, with a minimum TCO of less than 75 DU extending from the pole to 50˚S for the first
579 six years following the war. This depletion is not only seen in the SH polar region, but also the
580 NH polar region.
581   Surface UV is affected by both the O_3 loss, which increases surface UV, and the smoke
582 injection, which decreases surface UV. For the regional war, the smoke injection is small enough
583 relative to the O_3 destruction that there is an increase in surface UV for the entire period
584 following the war that is proportional to the amount of the O_3 loss. For the global war, while the
585 O_3 loss is extremely large, the smoke injection is so big that it leads to reduced UV at the surface
586 for the first few years following the war. The rate of O_3 recovery lags the smoke removal and
587 thus there are several years of very high surface UV, with a UV Index over 35 following a global
588 nuclear war. Thus, following a regional war the climatic changes and the surface UV changes
589 occur at the same time, shortening the period of large change and providing a uniform threat that
590 decreases with time. However, for the global war the climatic changes come first followed by the
591 elevated surface UV. This extends the period of changed conditions and causes the nature of the
592 change to switch from reduced light, surface temperature and precipitation to one of increased
593 surface UV. This means that adaptions that may have worked in first few years following the
594 global war may not work as the surface UV increases. Changes in spectral integrals show that
595 greatest increase is for DNA damage, which increases by up to 140% in the global war case and
596 there is a risk of insufficient vitamin-D during the first few years following a global war.
597 Assessments of impacts on agriculture and fisheries like those done by Jägermeyr et al. (2020)
598 and Scherrer et al. (2020) for a regional nuclear war need to include the effects of UV and
599 surface O_3 changes, and need to be done for the larger and differently sequenced effects that are
600 generated by a global nuclear war.
601   A new version of the WACCM model has been released (Gettelman et al., 2019) with
602 improved atmospheric physics including interactive modal aerosols, stratospheric aerosols, a new
603 boundary layer and shallow convection scheme, a new cloud scheme that includes the aerosol
604 indirect effect, and improved biogeochemistry in the land and the ocean models. Initial
605 experiments with this model have shown it to be unstable when presented with the large
606 perturbation considered here, so further work is needed before using it for nuclear war
607 simulations. We also plan to explore the addition of organic and sulfate coatings on the soot. Yu
608 et al. (2019, 2020) have shown that wildfire smoke lofted into the stratosphere is coated with
609 large amounts of organics. They also speculated on whether it might become coated in sulfate
610 and contribute surface area to heterogenous chemistry. Because of the different fuels, urban fires
611 (as in a nuclear war scenario) would likely have less of an organic coating than wildfire smoke,
612 but such a coating would provide a "lensing" effect that increases the particle absorption (Bond
613 et al., 2006) and the larger particles would likely have a shorter lifetime in the stratosphere. This
614 could affect both the intensity and the duration of climatic changes following a nuclear war.
615   The ability to calculate and output spectral action functions allows for a better assessment
616 of the threats posed to the biota by a nuclear war. It also opens up the possibility for these data to
617 be coupled with surface models allowing the effects of the detailed changes in surface light
618 spectra to be included in parameterizations of the effects on the biota including those for
619 phytoplankton and vegetation. There is a need for parameterizations of biological effects to be

developed for the large UV increases that are predicted here and for climatic conditions that are cooling rather than for the warming conditions that have generally been evaluated for studies of the ozone hole and anthropogenic climate change. Action spectra also provide data that can be used for assessment of human health impacts. These model improvements would be beneficial for simulation of other types of climate change driven by large aerosol injections including volcanic eruptions, mass fires, dust storms, and solar geoengineering.

Data

The CESM model is freely available from NCAR, but requires registration at www.cesm.ucar.edu/models/cesm1.2. All the data and scripts needed for the plots presented in this paper and the supplement are publicly available from osf.io/Bardeen_2021_OzoneUV (doi:10.17605/OSF.IO/KVY86). The full model output is very large and is stored on the PetaLibrary at the University of Colorado, which is not available to the public. However, additional data from these runs can be provided upon request.

Tables

Table 1. List of the WACCM4/CARMA simulations performed in this study and our prior work. IP indicates a regional conflict between India and Pakistan, and UR indicates a global conflict between the US and Russia. Soot shows the total soot emission, NO the total NO emission (fireball and fire), TUV indicates that in-line TUV was used for photolysis, and AOD indicates that the aerosol optical depth was included in the TUV photolysis calculation. Yields indicate the total yield, the count and size (Mt) of the individual weapons that are assumed for the NO_x production, and the source of the weapon inventory. For Toon et al. (2008), the weapon yield was assumed to be 300 kt rather than 100 kt. For NRC (1985), 1500 Mt of ground bursts were not included in the total. The different NO emission cases (NO, NO2, and NO3) are sensitivity tests that differ only in the amount and altitude extent of the fireball NO emission.

654   **Table 2.** List of the main chemical reactions used in WACCM that are important to odd-oxygen
655   (O and O_3) concentrations. These reactions are grouped by production and loss and by catalytic
656   cycles for analysis purposes. The weight indicates the net odd-oxygen production or loss from a
657   reaction. These weights are used to sum the individual reaction rates to calculate total production
658   and loss rates.
659

660   **Figures**

661   **Figure 1**. Evolution of the change in the global average vertical profile for soot (a, g),
662   temperature (b,h), H_2O (c, i), HO_x (d, j), NO_x (e, k), and O_3 (f, l) for the IP (top) and UR
663   (bottom) cases from the control. Soot, temperature, and H_2O are shown as differences, while
664   HO_x, NO_x, and O_3 are shown as percentage differences. Scales are the same for the IP and UR
665   cases. HO_x is the sum of H, OH, and HO_2, and NO_x is the sum of N, NO, and NO_2.

666   **Figure 2**. Evolution of the change in global average column O_3 for the 5 Tg soot injection
667   regional nuclear war cases: Mills et al. (2008), Mills et al. (2014), Toon et al. (2019), IP, IP–NO,
668   and IP–AOD. See Table 1 for the abbreviations and descriptions of the India/Pakistan (IP) cases
669   from this study.

670   **Figure 3**. Evolution of column integrated absolute chemical reaction rates (color) and the O_3
671   column (black) for the IP–AOD (left), IP (center), and IP-NO (right) cases. The total reaction
672   rates are on the top (a-c), and the percentage difference from the control case are on the bottom
673   (d-f). The IP–AOD case does not include aerosols in the photolysis and the IP-NO case does not
674   include any NO injection. The solid lines are the named case and the dotted lines are the control
675   case. See Table 2 for the reactions included in each grouping.

676   **Figure 4**. Similar to Figure 2, but for column integrated chemical reaction rates relative to the
677   evolving total production rate of the respective case. Thus, by definition the total production for
678   each of these cases, both the perturbation and the control, is 1.0.

679   **Figure 5**. Global average vertical profile of absolute reaction rates (colors) and O_3 (black) for the
680   first year following the war for the IP–AOD and IP cases. In both cases, the solid lines are the
681   named case and the dotted lines are the control. Note the O_3 scale is increasing to the left.

682   **Figure 6**. Evolution of the zonal average percent change in the O_3 column from the control for
683   the IP (left) and UR (right) cases.

684   **Figure 7**. Evolution of zonal and monthly averages of the daily maximum clear-sky surface UV
685   Index for the control (left), IP (middle), and UR (right) cases. The maximum values are 26, 33,
686   and 50 respectively. The gray line shows the UV Index of the 20 contour to highlight the
687   expansion of areas of extreme UV in the IP and UR cases.

688   **Figure 8**. Evolution of the change in global average column O_3 in the Northern Hemisphere from
689   Pittock et al. (1986) using scenarios from AMBIO (1982), Knox (1983), and NRC (1985) along
690   with WACCM4 simulations from Coupe et al. (2019), UR, UR-NO, UR-AOD, UR+NO2, and
691   UR+NO3 (left) and global averages (right) for just the WACCM4 simulations. Kao et al. (1990)
692   only provided information about the end of their 20-day simulation. See Table 1 for the
693   abbreviations and descriptions of the United States/Russia (UR) cases from this study.

694   **Figure 9**. Similar to Figure 3, but for the UR–AOD (left), UR (center), and UR-NO (right) cases.

695   **Figure 10**. Similar to Figure 4, but for the UR–AOD (left) and UR (right) cases.

696   **Figure 11**. Similar to Figure 5, but for the UR–AOD (left) and UR (right) cases. Note the O_3
697   scale is increasing toward the left in panels a and b.

698   **Figure 12**. Evolution of the change in the global average for surface values of aerosol optical
699   depth, temperature, O_3 column, and precipitation compared with the spectral integrals of PAR
700   and UV-B for the IP (left) and UR (right) cases. Temperature (black) is on the right scale and the
701   percentage change of the other fields (color) are on the left scale. AOD is the total aerosol optical
702   depth including both the soot and the background aerosol and has been reduced by a factor of 3
703   in the IP case and 30 in the UR case to fit on the plot. The maximum global average AOD values
704   are 0.13 for the control, 0.20 for the IP case, and 2.92 for the UR case.

705   **Figure 13**. Evolution of the change in the global average surface values for UV-B compared
706   with the action functions for plant growth, inhibition of phytoplankton, cataract formation,
707   vitamin-D synthesis, erythema, and DNA damage for the IP (left) and UR (right) cases. Note the
708   different vertical scales for the two panels.

709   **Figure 14**. UV spectra for O_3 absorption cross-section (black) and soot mass absorption
710   coefficient (gray) along with spectral weighting functions for UV-B, erythema, DNA damage,
711   and two metrics for non-melanoma skin cancer (colors) over the range 230-370 nm (left).
712   Evolution of the change in the global average spectral integrals of UV-B compared with the
713   action functions for erythema, DNA damage and non-melanoma skin cancer for the IP (center)
714   and UR (right) cases. Note the different vertical scales for these two panels.

715

716 **References**

717 Aleksandrov, V. V., & G. L. Stenchikov (1983), On the modeling of the climatic consequences
718   of the nuclear war. *Proc. Appl. Math*, 21 pp., Comput. Cent., Russ. Acad. of Sci.,
719   Moscow.

720 Allen, D. J., S. Nogués, & N. R. Baker (1998), Ozone depletion and increased UV-B radiation: is
721   there a real threat to photosynthesis?. *J. Exp. Bot.*, 49, 1775-1788,
722   doi:10.1093/jxb/49.328.1775.

723 Alves, R. N., & S. Agusti (2020), Effect of ultraviolet radiation (UVR) on the life stages of fish.
724   *Rev. Fish Biol. Fish.*, 30, 335-372.

725 Andreae. M. O. (2019), Emission of trace gases and aerosols from biomass burning – an updated
726   assessment. *Atmos. Chem. Phys.*, 19, 8523–8546, doi:10.5194/acp-19-8523-2019.

727 Andres, A., H.-J. Altheide, M. Knälmann, & H. Tronnier (1995), Action spectrum for erythema
728   in humans investigated with dye lasers. *Photochem. Photobiol.*, 61, 2000-2005, doi:
729   10.1111/j.1751-1097.1995.tb03961.x.

730 Ballaré, C. L., M. C. Rousseaux, P. S. Searles, J. G. Zahler. C. V. Giordano, M. Robson, et al.
731   (2001), Impacts of solar ultraviolet-B radiation on terrestrial ecosystems of Tierra del
732   Fuego (southern Argentina) An overview of recent progress. *J. Photochem. Photobiol. B:*
733   *Biology*, 62, 67–77, doi:10.1016/S1011-1344(01)00152-X.

734 Ballaré, C. L., M. M., Caldwell, S. D. Flint, S. A. Robinson, & J. F. Bornman (2011), Effects of
735   solar ultraviolet radiation on terrestrial ecosystems: Patterns, mechanisms, and
736   interactions with climate change. *Photochem. Photobiol. Sci.*, 10, 226-241, doi:
737   10.1039/C0PP90035D.

738 Bardeen C. G., O. B. Toon, E. J. Jensen, D. R. Marsh, & V. L. Harvey (2008), Numerical
739   simulations of the three-dimensional distribution of meteoric dust in the mesosphere and
740   upper stratosphere. *J. Geophys. Res.,* 113: D17202, doi:10.1029/2007JD009515.

741 Bardeen, C. G., R. R. Garcia, O. B. Toon, & A, J. Conley (2017), On transient climate change at
742   the Cretaceous−Paleogene boundary due to atmospheric soot injections. *Proc. Natl. Acad.*
743   *Sci. U. S. A.*, 114, E7415-E7424, doi:10.1073/pnas.1708980114.

744 Bassman, J. H. (2004), Ecosystem consequences of enhanced solar ultraviolet radiation:
745   secondary plant metabolites as mediators of multiple trophic interactions in terrestrial
746   plant communities. *Photochemistry and Photobiology*, 79, 382–398, doi:10.1111/j.1751-
747   1097.2004.tb00025.x.

748 Bonan, G. B., P. J. Lawrence, K. W. Oleson, S. Levis, M. Jung, M. Reichstein, D. M. Lawrence,
749   & S. C. Swenson (2011), Improving canopy processes in the Community Land Model
750   version 4 (CLM4) using global flux fields empirically inferred from FLUXNET data. *J.*
751   *Geophys. Res.*, 116, G02014, doi:10.1029/2010JG001593.

752 Bond, T. C., G. Habib, and R. W. Bergstrom (2006), Limitations in the enhancement of visible
753   light absorption due to mixing state. *J. Geophys. Res.*, 111, D20,
754   doi:10.1029/2006JD007315.

755 Bornman, J. F., P. W. Barnes, S. A. Robinson, C. L. Ballaré, S. D. Flint, & M. M. Caldwell
756   (2015), Solar ultraviolet radiation and ozone depletion-driven climate change: effects on

757 terrestrial ecosystems. *Photochem. Photobiol. Sci.*, 14, 88-107,
758   doi:10.1039/C4PP90034K.

759 Brasseur, G. P., & S. Solomon (2005), *Aeronomy of the Middle Atmosphere, 3rd ed.*
760   Netherlands, Springer, doi: 10.1007/1-4020-3824-0.

761 Boucher, N., B. B. Prézelin, T. Evens, R. Jovine, B. Kroon, M. A. Moline, & O. Schofield
762   (1994) Icecolors '93: Biological weighting function for the ultraviolet inhibition of carbon
763   fixation in a natural Antarctic phytoplankton community. *Antarct. J. Rev.*, 272-274.

764 Bouillon, R., J. Eisman, M. Garabedian, M. F. Holick, J. Kleinschmidt, T. Suda, I. Terenetskaya
765   & A. R. Webb (2006), Action spectrum for the production of previtamin D3 in human
766   skin. *International Commission on Illumination*, technical report 174.
767 Chabrillat, S., & G. Kockarts (1997), Simple parameterization of the absorption of the solar
768   Lyman-alpha line. *Geophys. Res. Lett.*, 24, 2659-2662, doi:10.1029/97GL52690.

769 Chabrillat, S., & G. Kockarts (1998), Correction to "Simple parameterization of the absorption of
770   the solar Lyman-alpha line", *Geophys. Res. Lett.*, 25, 1, 79, doi:10.1029/97GL03569.

771 Chang, J. S. W. H. Duewer, & D. J. Wuebbles (1979), The atmospheric nuclear test of the 1950s
772   and 1960s: a possible test of ozone depletion theories. *J. Geophys. Res.*, 84, 1755-1765,
773   doi:10.1029/JC084iC04p01755.

774 Chang, J. S. & D. J. Wuebbles (1984), Nuclear Explosions and Atmospheric Ozone. In J.
775   London & G. F. White (Eds.), *The Environmental Effects of Nuclear War*, AAAS
776   Selected Symposium (98, pp. 79-95). Boulder, CO: Westview Press, Inc.

777 Commission Internationale de l'Eclairage (2006), Photocarcinogenesis Action Spectrum (Non-
778   Melanoma Skin Cancers), CIE S 019/E:2006, Vienna.

779 Coupe, J., C. G. Bardeen, A. Robock, & O. B. Toon (2019), Nuclear winter responses to nuclear
780   war between the United States and Russia in the Whole Atmosphere Community Climate
781   Model Version 4 and the Goddard Institute for Space Studies ModelE. *J. Geophys. Res.*,
782   124, 8522-8543, doi.org/10.1029/2019JD030509.

783 Coupe, J., S. Stevenson, N. S. Lovenduski, T. Rohr, C. S. Harrison, A. Robock, et al. (2021),
784   Nuclear Niño response observed in simulations of nuclear war scenarios. *Commun. Earth
785   Environ.*, 2, doi:10.1038/s43247-020-00088-1.

786 Covey, C., S. H. Schneider, & S. L. Thompson (1984), Global atmospheric effects of massive
787   smoke injections from a nuclear war: results from general circulation model simulations.
788   *Nature*, 308, 21-25, doi: 10.1038/308021a0.

789 Crutzen, P. J. (1970), The influence of nitrogen oxide on the atmospheric ozone content. *Q. J. R.
790   Meteorol. Soc.*, 96, 320–327, doi:10.1002/qj.49709640815.

791 Crutzen, P. J. & J. W. Birks (1982), The atmosphere after a nuclear war: twilight at noon. *Ambio*,
792   XI, 114-125.

793 Danabasoglu, G., Bates, S. C., Briegleb, B. P., Jayne, S. R., Jochum, M., Large, W. G., et al.
794   (2012), The CCSM4 ocean component. *J. Clim.*, 25, 1361–1389, doi:10.1175/JCLI-D-11-
795   00091.1.

796 de Gruiji, F. R., and J. C. Van der Leun (1994), Estimate of the wavelength dependency of
797   ultraviolet carcinogenesis in humans and its relevance to the risk assessment of a
798   stratospheric ozone depletion. *Health Phys.*, 67, 319-325, doi:10.1097/00004032-
799   199410000-00001.

800 De Tommasi, E. D., R. Congestri, P. Dardano, A. Chiara De Luca, S. Managò, I. Rea, & M. De
801   Stefano (2018), UV-shielding and wavelength conversion by centric diatom
802   nanopatterned frustules. *Sci. Rep.*, 8, 16285 (2018), doi: 10.1038/s41598-018-34651-w.

803 Emberson, L. D., H. Pleijel, E. A. Ainsworth. M. van den Berg, W. Ren, S. Osborne, et al.
804   (2018), Ozone effects on crops and consideration in crop models. *Eur. J. Agron.*, 100, 19-
805   34, doi:10.1016/j.eja.2018.06.002.

806 Flint, S. D. & M. M. Caldwell (2001), A biological spectral weighting function for ozone
807   depletion research with higher plants. *Physiol. Plant.*, 117, 137–144, doi:10.1034/j.1399-
808   3054.2003.1170117.x.

809 Foley, H. M. & M. A. Ruderman (1973), Stratospheric NO production from past nuclear
810   explosions. *J. Geophys. Res.*, 78, 4441-4554, doi: 10.1029/JC078i021p04441.

811 Forrest, K. Y. Z., & Stuhldreher, W. L. (2011). Prevalence and correlates of vitamin D
812   deficiency in US adults. *Nutrition Research (New York, N.Y.)*, *31*(1), 48–54. doi:
813   10.1016/j.nutres.2010.12.001

814 Froidevaux, L., D. E. Kinnison, R. Wang, J. Anderson, & R. A. Fuller (2019), Evaluation of
815   CESM1 (WACCM) free-running and specified-dynamics atmospheric composition
816   simulations using global multi-species satellite data records, *Atmos. Chem. Phys.*, 19,
817   4783-4821, doi:10.5194/acp-19-4783-2019.

818 Gettelman, A., M. J. Mills, D. E. Kinnison, R. R. Garcia, A. K. Smith, D. R. Marsh, et al. (2019),
819   The Whole Atmosphere Community Climate Model Version 6 (WACCM6), *J. Geophys.*
820   *Res.*, 124, 12380-12403, doi:10.1029/2019JD030943.

821 Glasstone, S., & Dolan, P J. (1977), *The Effects of Nuclear Weapons*. Third edition. United
822   States, doi:10.2172/6852629.

823 Gorshelev, V., A. Serdyuchenko, M. Weber, W. Chehade, & J. P. Burrows (2014), High spectral
824   resolution ozone absorption cross-sections – Part 1: Measurements, data analysis and
825   comparison with previous measurements around 293 K. *Atmos. Meas. Tech.*, 7, 609–624,
826   doi:10.5194/amt-7-609-2014.

827 Hakala-Yatkin, M., M. Mäntysaari, H. Mattila, & E. Tyystjärvi (2010), Contributions of visible
828   and ultraviolet parts of sunlight to photoinhibition. *Plant Cell Physiol.*, 51, 1745-1753,
829   doi:10.1093/pcp/pcq133.

830 Harwell, M. A. & T. C. Hutchinson (1986), *Environmental Consequences of Nuclear War*
831   *Volume II: Ecological and Agricultural Effects*. (SCOPE; 28) New York: John Wiley &
832   Sons Ltd.

833 Hurrell, J. W. *et al*. (2013), The Community Earth System Model: A Framework for
834   Collaborative Research. *Bull. Amer. Met. Soc.*, 94, 1339-1360, doi:10.1175/BAMS-D-12-
835   00121.1.

836 Iacono, M. J., E. J. Mlawer, S. A. Clough, and J.-J. Morcette (2000), Impact of an improved
837   longwave radiation model, RRTM, on the energy budget and thermodynamic properties
838   of the NCAR community climate mode, CCM3. *J. Geophys. Res.*, 105, 14873–14890,
839   doi:10.1029/2000JD900091.

840 Jägermeyr, J., A. Robock, J. Elliot, C. Müller, L. Xia, N. Khabarov, et al. (2020), A regional
841   nuclear conflict would compromise global food security. *Proc. Natl. Acad. Sci. U. S. A.*,
842   117, 7071-7081, doi:10.1073/pnas.1919049117.

843 Jeffrey, S. W., H. S. MacTavish, W. C. Dunlap, M. Vask, & K. Groenwoud (1999), Occurrence
844   of UVA- and UVB-absorbing compounds in 152 species (206 strains) of marine
845   microalgae. *Mar. Ecol. Prog. Ser.*, 189, 35-51.

846 Kao, C. Y. J., G. A. Glatzmaier, R. C. Malone, & R. P. Turco (1990), Global 3-dimensional
847   simulations of ozone depletion under postwar conditions. *J. Geophys. Res.*, 95, 22495–
848   22512, doi: 10.1029/JD095iD13p22495.

849 Kataria, S., A. Jajoo, & K. N. Guruprasad (2014), Impact of increasing Ultraviolet-B (UV-B)
850   radiation on photosynthetic processes. *J. Photochem. Photobiol. B*, 137, 55-66, doi:
851   10.1016/j.jphotobiol.2014.02.004.

852 Koppers, G. A. A., & D. P. Murtagh (1996), Model studies of the influence of O_2 photodissociation
853   parameterizations in the Schumann-Runge bands on ozone related photolysis in the upper
854   atmosphere, *Ann. Geohysicae*, 14, 68-79, doi:10.1007/s00585-996-0068-9.

855 Krizek, D. T. (2004), Influence of PAR and UV-A in determining plant sensitivity and
856   photomorphogenic responses to UV-B radiation, *Photochem. Photobiol.*, 79, 307-325,
857   doi:10.1562/2004-01-27-ir.1.

858 Kristensen, H. M. & M. Korda (2020a), United States nuclear forces, 2020. *Bull. At. Sci.*, 76, 46-
859   60, doi:10.1080/00963402.2019.1701286.

860 Kristensen, H. M. & M. Korda (2020b), Russian nuclear forces, 2020. *Bull. At. Sci.*, 76, 102-117,
861   doi:10.1080/00963402.2020.1728985.

862 Lewis, K. N. (1979), The prompt and delayed effects of nuclear war. *Sci. Am.*, 241, 35-47.

863 Lindsay, K., G. B. Bonan, S. C. Doney, F. M. Hoffman, D. M. Lawrence, M. C. Long, et al.
864   (2014), Preindustrial-control and twentieth-century carbon cycle experiments with the
865   Earth System Model CESM1(BGC). *J. Clim.*, 27, 8981-9005, doi:10.1175/JCLI-D-12-
866   00565.1.

867 Llabrés, M., S. Agusti, M. Fernández, A. Canepa, F. Maurin, F. Vidal, & C. M. Duarte (2013),
868   Impact of elevated UVB radiation on marine biota: a meta-analysis. *Glob. Ecol.
869   Biogeogr.*, 22, 131-144, doi:10.1111/j.1466-8238.2012.00784.x.

870 Lombardozzi, D., J. P. Sparks, G. Bonan, & S. Levis (2012), Ozone exposure causes a
871   decoupling of conductance and photosynthesis: implications for the Ball-Berry stomatal
872   conductance model. *Oecologia*, 169, 651-659, doi:10.1007/s00442-011-2242-3.

873 Lombardozzi, D., J. P. Sparks, & G. Bonan (2013), Integrating O3 influences on terrestrial
874   processes: photosynthetic and stomatal response data available for regional and global
875   modeling. *Biogeosciences*, 10, 6815–6831, doi:10.5194/bg-10-6815-2013.

876 Lombardozzi, D., S. Levis, G. Bonan, P. G. Hess, & J. P. Sparks (2015), The influence of
877   chronic ozone exposure on global carbon and water cycles. *J. Clim.*, 28, 292-305,
878   doi:10.1175/JCLI-D-14-00223.1

879 Lovenduski, N. S., C. S. Harrison, H. Olivarez, C. G. Bardeen, O. B. Toon, J. Coupe, et al.
880   (2020), The potential impact of nuclear conflict on ocean acidification, *Geophys. Res.*
881   *Letts.*, 47, e2019GL086246, doi:10.1029/2019GL086246.

882 Madronich, S., & S. Flocke (1997), Theoretical estimation of biologically effective UV radiation
883   at the Earth's surface, in *Solar Ultraviolet Radiation-Modeling, Measurements and*
884   *Effects*, NATO ASI Ser., vol. I52, edited by C. Zerefos, pp. 23–48, Springer, Berlin,
885   Germany.

886 Malone R. C., L. H. Auer, G. A. Glatzmaier, M. C. Wood, & O. B. Toon (1986), Nuclear winter:
887   3-dimensional simulations including interactive transport, scavenging, and solar heating
888   of smoke. *J. Geophys. Res.*, 91, 1039–1053, doi:10.1029/JD091iD01p01039.

889 Marsh, D.R., M. J. Mills, D. E. Kinnison, J.-F. Lamarquem N. Calvo, & L. M. Polvani (2013),
890   Climate change from 1850 to 2005 simulated in CESM1(WACCM). *J. Clim.*, 26, 7372-
891   7391, doi:10.1175/JCLI-D-12-00558.1.

892 Mills, M. J., O. B. Toon, R. P. Turco, D. E. Kinnison, & R. R. Garcia (2008), Massive global
893   ozone loss predicted following regional nuclear conflict. *Proc. Natl. Acad. Sci. U.S.A.,*
894   105**:**5307–5312, doi:10.1073/pnas.0710058105.

895 Mills, M. J., O. B. Toon, J. Lee-Taylor, & A. Robock (2014), Multidecadal global cooling and
896   unprecedented ozone loss following a regional nuclear conflict. *Earth's Future,* 2, 161-
897   176, doi:10.1002/2013EF000205.

898 Minschwaner, K., & D. E. Siskind (1993), A new calculation of nitric oxide photolysis in the
899   stratosphere, mesosphere, and lower thermosphere, *J. Geophys. Res.*, 98, 20401-20412,
900   doi:10.1029/93JD02007.

901 Molina, M. J., L. T. Molina, T. B. Fitzpatrick, & P. T. Nghiem (2000), Ozone depletion and human
902   health effects, *Environmental Medicine*, edited by L. Möller, pp. 28-51, Fälth & Hassler,
903   Sweden.

904 National Academy of Sciences (1975), *Long-term Worldwide Effects of Multiple Nuclear*
905   *Weapons*, Washington, D.C.: National Academy of Sciences Press, doi:10.17226/20139.

906 National Resource Council (1984), *Causes and Effects of Changes in Stratospheric Ozone:*
907   *Update 1983*. Washington, D.C: National Academy Press, doi:10.17226/19330.

908 National Resource Council (1985), *The Effects on the Atmosphere of a Major Nuclear Exchange*.
909   Washington, D.C.: National Academy Press, doi:10.17226/540.

910 Oleson, K.W., D. M. Lawrence, G. B. Bonan, M. G. Flanner, E. Kluzek, P. J. Lawrence, et al.
911   (2010), *Technical Description of version 4.0 of the Community Land Model (CLM)*,
912   NCAR/TN-478+STR.

913 Oriowo, O. M., A. P. Cullen, B. R. Chou, & J. G. Sivak (2001), Action spectrum and recovery
914   for in vitro UV-induced cataract using whole lenses. *Investig. Ophthalmol. Vis. Sci.*, 42,
915   2596-2602.

916   Office of Technology Assessment (1979), *The Effects of Nuclear War*, OTA-NS-89, U.S.
917   Government Printing Office, 151 pp., 1979.

918   Para, R., E. Cadena & C. Flores (2019), Maximum UV Index records (2010–2014) in Quito
919   (Ecuador) and its trend inferred from remote sensing data (1979–2018). *Atmosphere*, 10,
920   787, doi:10.3390/atmos10120787.

921   Pierazzo, E., R. R. Garcia, D. E. Kinnison, D. R. Marsh, and P. J. Crutzen (2010), Ozone
922   perturbation from medium-size asteroid impacts in the ocean. *Earth Planet. Sci. Lett.*,
923   299, 263–272, doi:10.1016/j.epsl.2010.08.036.

924   Pittock, A. B., T. P. Ackerman, P. J. Crutzen, M. C. MacCracken, C. S. Shapiro & R. P. Turco
925   (1986), *Environmental Consequences of Nuclear War Volume I: Physical and*
926   *Atmospheric Effects*. (SCOPE; 28) New York: John Wiley & Sons Ltd,
927   doi:10.1002/joc.3370070112.

928   Polvani, L. M., M. Abalos, R. Garcia, D. E. Kinnison, & W. J. Randel (2017), Significant
929   weakening of Brewer-Dobson circulation trend over the 21st century as a consequence of
930   the Montreal Protocol, *Geophys. Res. Lett.*, 45, 401-409, doi:10.1002/2017GL075345.

931   Ragni, M., R. L. Airs, N. Leonardos, & R. J. Geider (2008), Photoinhibition of PSII in *emiliania*
932   *huxleyi* (haptophyta) under high light stress: The roles of photoacclimation,
933   photoprotection, and photorepair. *J. Phycol.*, 44, 670-683, doi:10.1111/j.1529-
934   8817.2008.00524.x.

935   Randel, W. J., L. Polvani, F. Wu, D. E. Kinnison, C.-Z. Zou, & C. Mears (2017), Troposphere-
936   stratosphere temperature trends derived from satellite data compared with ensemble
937   simulations from WACCM, *J. Geophys. Res.*, 122, 9651-9667,
938   doi:10.1002/2017JD027158.

939   Robock, A. (2002), The Climatic Aftermath. Science, 295, 1242-1244,
940   doi:10.1126/science.1069903.

941   Robock, A., L. Oman, G. L. Stenchikov, O. B. Toon, C. Bardeen, & R. P. Turco (2007a),
942   Climatic consequences of regional nuclear conflicts. *Atmos. Chem. Phys.*, 7, 2003–2012,
943   doi:10.5194/acp-7-2003-2007.

944   Robock, A., L. Oman, & G. L. Stenchikov (2007b), Nuclear winter revisited with a modern
945   climate model and current nuclear arsenals: Still catastrophic consequences. *J. Geophys.*
946   *Res.,* 112:D13107, doi:10.1029/2006JD008235.

947   Sample, A., & Y.-H. He (2018), Mechanisms and prevention of UV-induced melanoma.
948   *Photodermatol Photoimmunol Photomed.*, 34, 13-24, doi:10.1111/phpp.12329.

949   Schauberger, B., S. Rolinski, S. Schaphoff, & C. Müller (2019), Global historical soybean and
950   wheat yield loss estimates from ozone pollution considering water and temperature as
951   modifying effects. *Agric. For. Meteorol.*, 265, 1-15,
952   doi:10.1016/j.agrformet.2018.11.004.

953   Scherrer K. J. N., C. S. Harrison, R. F. Heneghan, E. Galbraith, C. G. Bardeen, et al. (2020),
954   Marine wild-capture fisheries after nuclear war. *Proc. Natl. Acad. Sci. U. S. A.*, 117,
955   29748-29758, doi:10.1073/pnas.2008256117.

956 Searles, P. S., S. D. Flint, & M. M. Caldwell (2001), A meta-analysis of plant field studies
957   simulating stratospheric ozone depletion. *Oecologia*., 127, 1–10,
958   doi:10.1007/s004420000592.

959 Setlow, R. B. (1974) The wavelengths in sunlight effective in producing skin cancer: A
960   theoretical analysis. *Proc. Nat. Acad. Sci. U. S. A.*, 71, 3363-3366,
961   doi:10.1073/pnas.71.9.3363.

962 Solomon, S. (1999) Stratospheric ozone depletion: A review of concepts and history. *Rev.*
963   *Geophys.*, 37, 275–316, doi:10.1029/1999RG900008.
964 Solomon, S., D. J. Ivy, D. E. Kinnison, M. J. Mills, R. R. Neely III, & A. Schmidt (2016),
965   Emergence of healing in the Antarctic ozone layer, *Science*, 353, 269-274,
966   doi:10.1126/science.aae0061.

967 Stenke, A., C. R. Hoyle, B. Luo, E. Rozanov, J. Gröbner, L. Maag, S. Brönnimann, & T. Peter
968   (2013), Climate and chemistry effects of a regional scale nuclear conflict. *Atmos. Chem.*
969   *Phys.*, 13, 9713–9729, doi:10.5194/acp-13-9713-2013.

970 Stock, C. A., J. G. John, R. R. Rykaczewski, R. G. Asch, W. L. Cheung, J. P. Dunne, et al.
971   (2017), Reconciling fisheries catch and ocean productivity. *Proc. Natl. Acad. Sci. U. S.*
972   *A.*, 114, E1441-E1449, doi:10.1073/pnas.1610238114.

973 Stone, K. A., S. Solomon, & D. E. Kinnison (2018), On the identification of ozone
974   recovery. *Geophys. Res. Lett.*, 45, 5158-5165, doi:10.1029/2018GL077955.

975 Toon, O. B., R. P. Turco, D. Westphal, R. Malone, & M. S. Liu (1988), A multidimensional
976   model for aerosols; Description of computational analogs. *J. Atmos. Sci.*, 54, 2123-2143,
977   doi:10.1175/1520-0469(1988)045<2123:AMMFAD>2.0.CO;2.

978 Toon, O. B., A. Robock, & R. P. Turco (2008), Environmental consequences of nuclear war.
979   *Phys. Today*, 61, 37–42, doi:10.1063/1.3047679.

980 Toon, O. B., C. G. Bardeen, A. Robock, L. Xia, H. Kristensen, M. McKinzie, et al. (2019),
981   Rapidly expanding nuclear arsenals in Pakistan and India portend regional and global
982   catastrophe. *Sci. Adv.*, 10, eaay5478, doi:10.1126/sciadv.aay5478.

983 Turco, R. P., O. B. Toon, T. P. Ackerman, J. B. Pollack, & C. Sagan (1983), Nuclear Winter:
984   Global consequences of multiple nuclear explosions. *Science*, 222, 1283-1292,
985   doi:10.1126/science.222.4630.1283.

986 Wagman, B., K. A. Lundquist, Q. Tang, L. G. Glascoe, & D. C. Bader (2020), Examining the
987   climate effects of a regional nuclear weapons exchange using a multiscale atmospheric
988   modeling approach. *J. Geophys. Res.*, 125, e2020JD033056, doi:10.1029/2020JD033056.

989 Wargent, J. J., & B. R. Jordan (2013), From ozone depletion to agriculture: understanding the
990   role of UV radiation in sustainable crop production. *New Phytol.*, 197, 1058-1076,
991   doi:10.1111/nph.12132.

992 World Health Organization (2002), *Global Solar UV Index: A Practical Guide*. World Health
993   Org., Geneva, Switzerland.

994 Xia, L., P. J. Nowack, A. Robock, & S. Tilmes (2017), Impacts of stratospheric sulfate
995   geoengineering on tropospheric ozone. *Atmos. Chem. Phys.*, 17, 11,913-11,928,
996   doi:10.5194/acp-17-11913-2017.

997 Xu, J. L. T. Bach, K. G. Schulz, W. Zhao, K. Gao, & U. Riebessell (2016), The role of coccoliths
998   in protecting *Emiliania huxleyi* against stressful light and UV radiation. *Biogeosciences*,
999   13, 4637–4643, doi:10.5194/bg-13-4637-2016.

1000 Yu, P., O. B. Toon, C. G. Bardeen, Y. Zhu, K. H. Rosenlof, R. W. Portmann, et al. (2019), Black
1001   carbon lofts wildfire smoke high into the stratosphere to form a persistent plume.
1002   Science, 365, 587-590, doi:10.1126/science.aax1748.

1003 Yu, P., S. M. Davis, O. B. Toon, R. W. Portmann, C. G. Bardeen, J. E. Barnes, et al. (2020),
1004   Persistent Stratospheric Warming Due to 2019-2020 Australian Wildfire Smoke,
1005   *Geophys. Res. Lett.*, 48, e92609, doi: 10.1029/2021GL092609.

1006

1007

1008
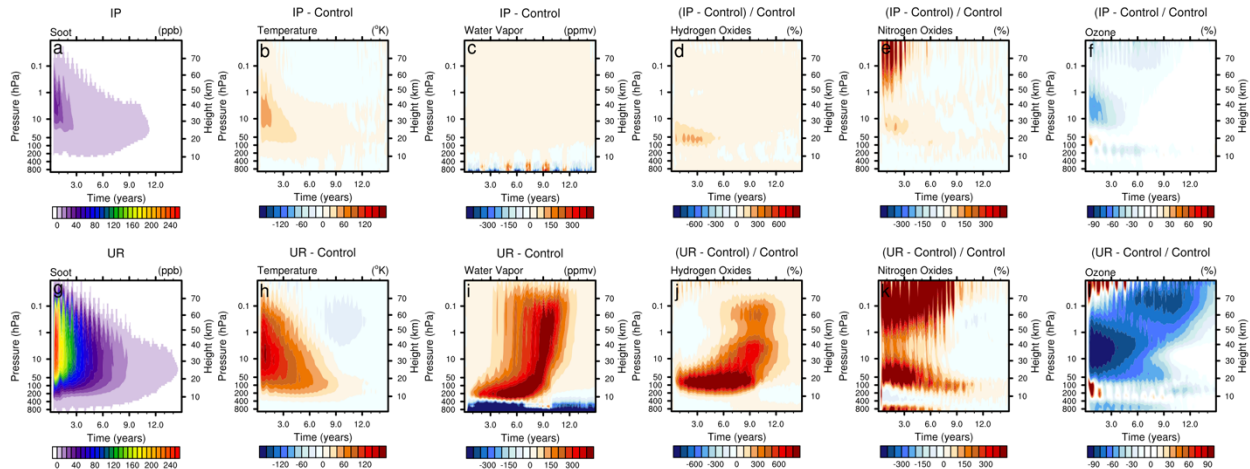
Figure 1. Evolution of the change in the global average vertical profile for soot (a, g), temperature (b,h), H_2O (c, i), HO_x (d, j), NO_x (e, k), and O_3 (f, l) for the IP (top) and UR (bottom) cases from the control. Soot, temperature, and H_2O are shown as differences, while HO_x, NO_x, and O_3 are shown as percentage differences. Scales are the same for the IP and UR cases. HO_x is the sum of H, OH, and HO_2, and NO_x is the sum of N, NO, and NO_2.
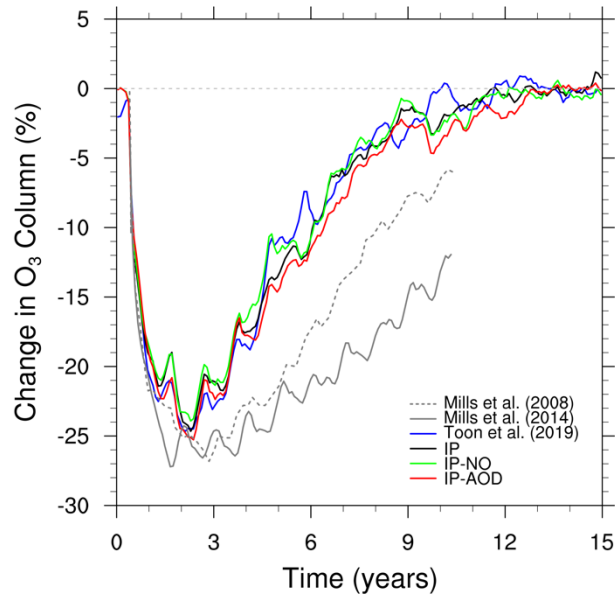
1016

Figure 2. Evolution of the change in global average column O_3 for the 5 Tg soot injection
       regional nuclear war cases: Mills et al. (2008), Mills et al. (2014), Toon et al. (2019), IP,
       IP–NO, and IP–AOD. See Table 1 for the abbreviations and descriptions of the
       India/Pakistan (IP) cases from this study.

1022

1023
1024 **Figure 3**. Evolution of column integrated absolute chemical reaction rates (color) and the
1025 O$_3$ column (black) for the IP–AOD (left), IP (center), and IP-NO (right) cases. The total
1026 reaction rates are on the top (a-c), and the percentage difference from the control case are
1027 on the bottom (d-f). The IP–AOD case does not include aerosols in the photolysis and the
1028 IP-NO case does not include any NO injection. The solid lines are the named case and the
1029 dotted lines are the control case. See Table 2 for the reactions included in each grouping.
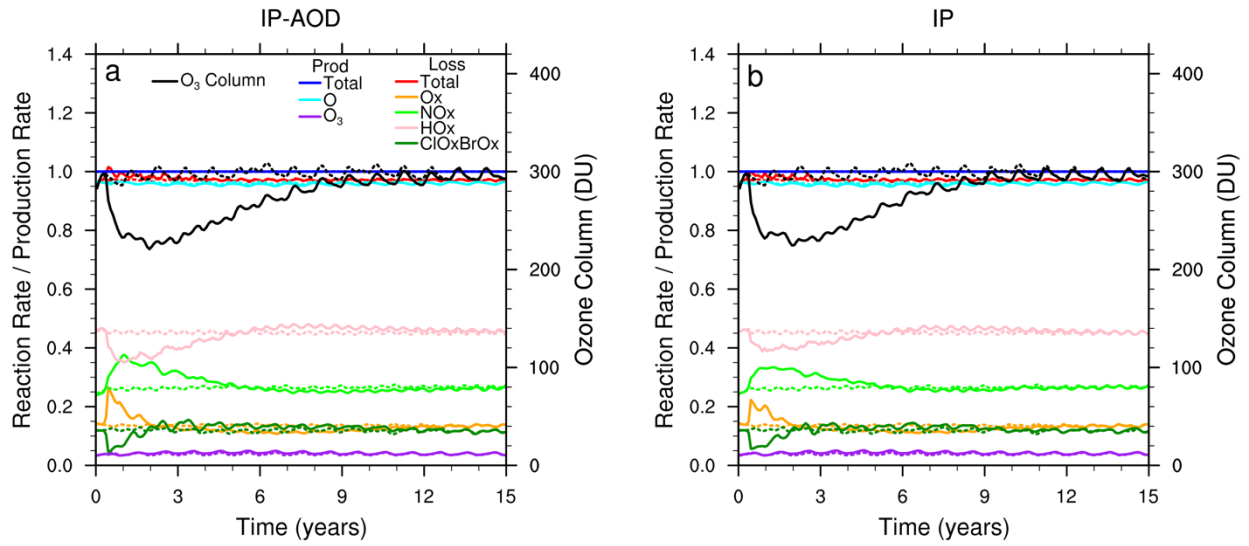
1030

1031

1032
1033

Figure 4. Similar to Figure 2, but for column integrated chemical reaction rates relative to the evolving total production rate of the respective case. Thus, by definition the total production for each of these cases, both the perturbation and the control, is 1.0.
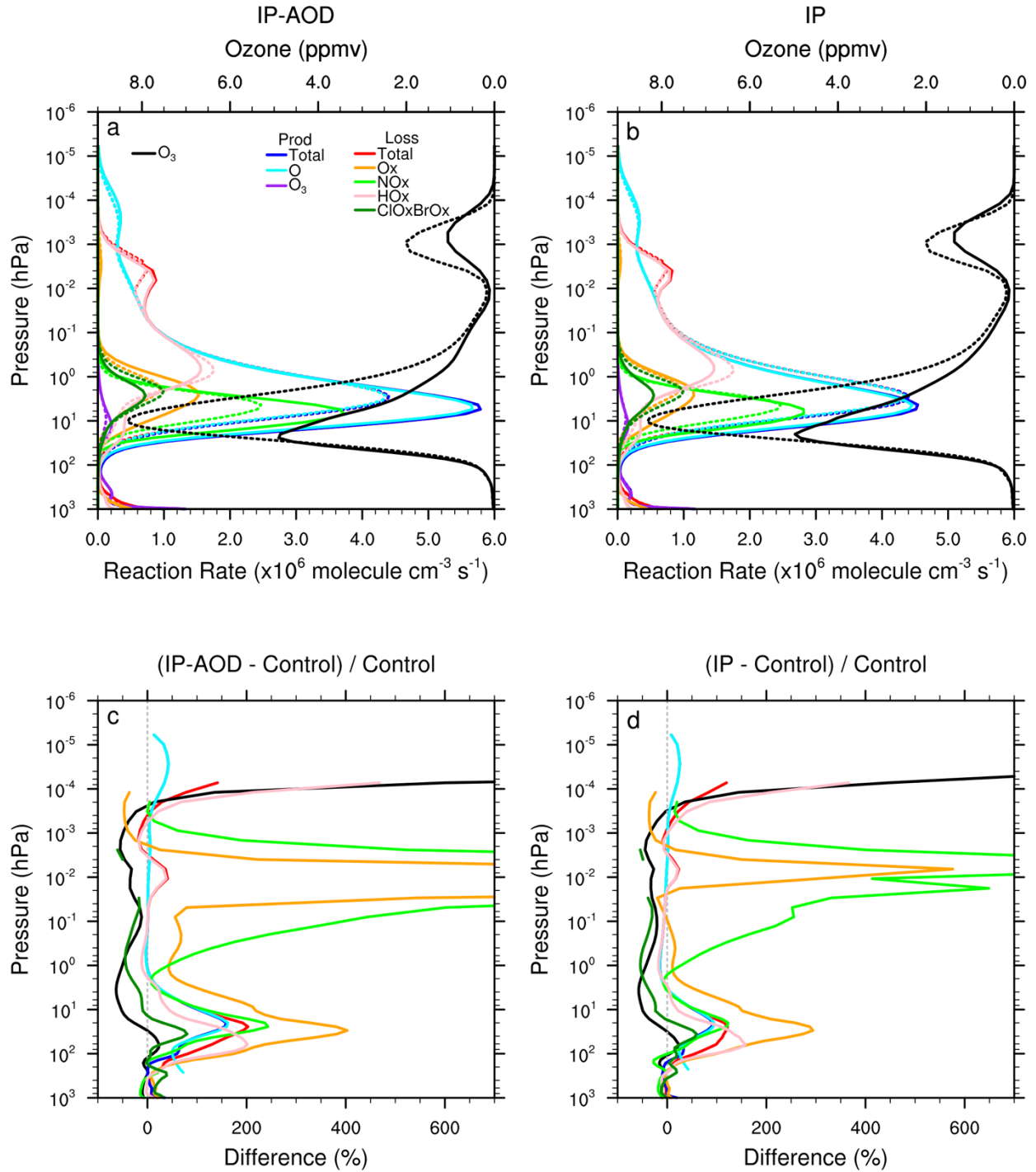
Figure 5. Global average vertical profile of absolute reaction rates (colors) and O_3 (black) for the first year following the war for the IP–AOD and IP cases. In both cases, the solid lines are the named case and the dotted lines are the control. Note the O_3 scale is increasing to the left.

1045

Figure 6. Evolution of the zonal average percent change in the O_3 column from the control for the IP (left) and UR (right) cases.
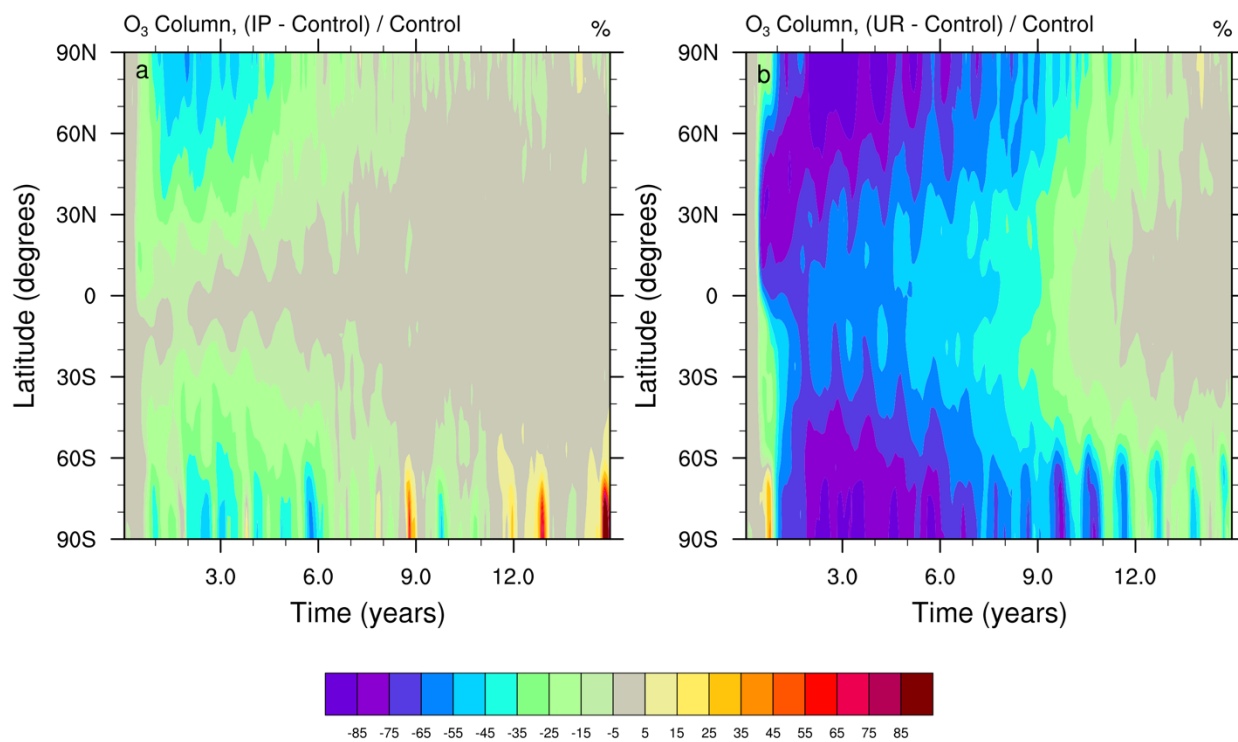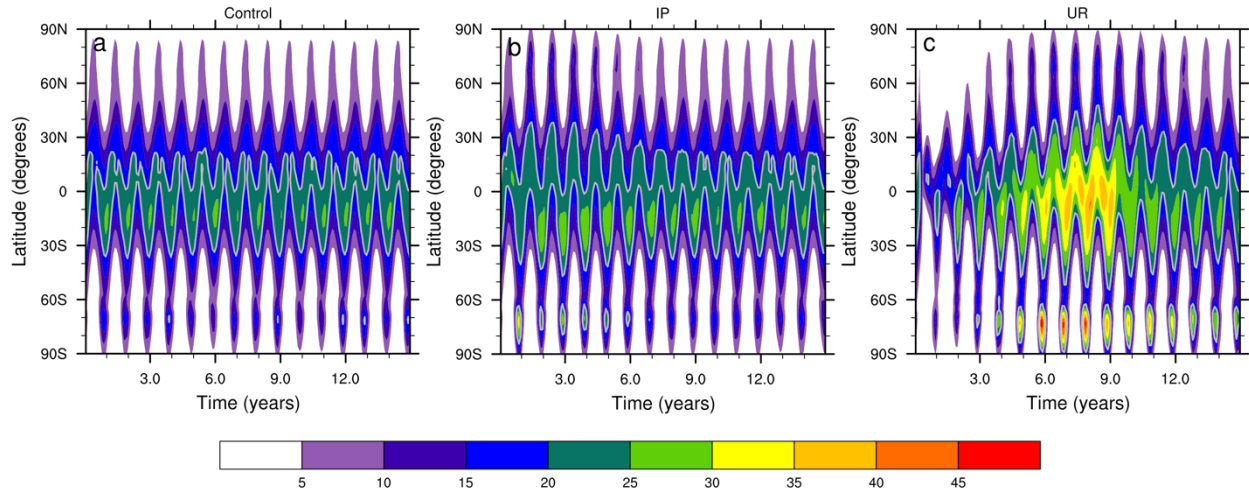
1046
1047
1048
1049

Figure 7. Evolution of zonal and monthly averages of the daily maximum clear-sky surface UV Index for the control (left), IP (middle), and UR (right) cases. The maximum values are 26, 33, and 50 respectively. The gray line shows the UV Index of the 20 contour to highlight the expansion of areas of extreme UV in the IP and UR cases.
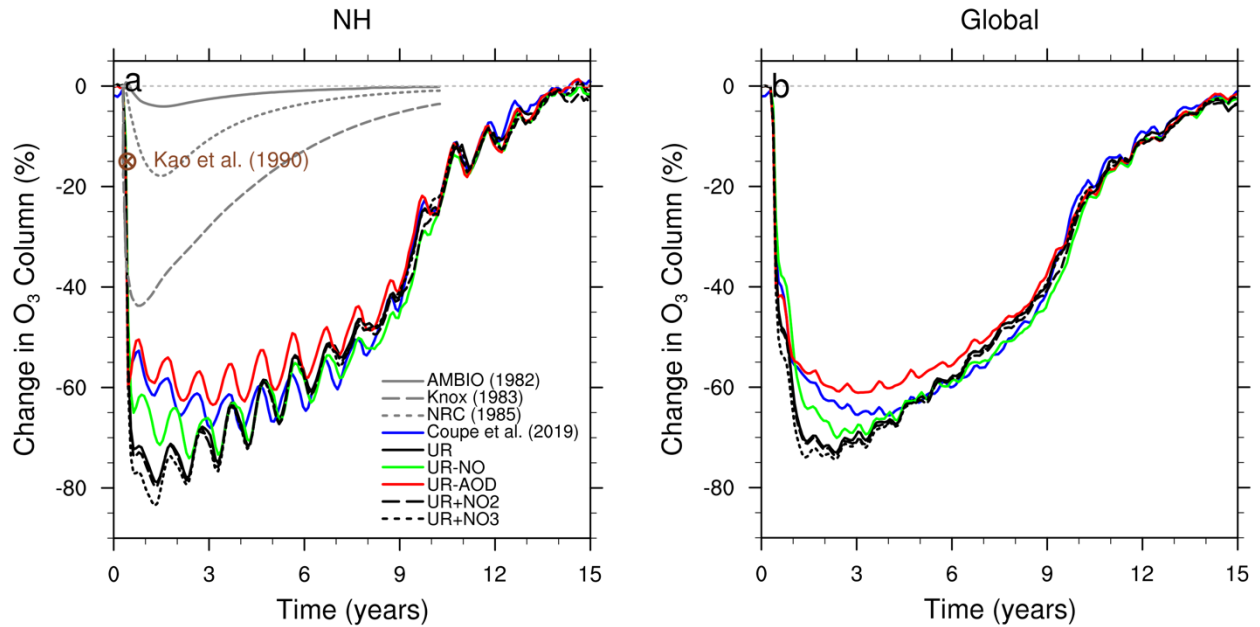
Figure 8. Evolution of the change in global average column O_3 in the Northern Hemisphere from Pittock et al. (1986) using scenarios from AMBIO (1982), Knox (1983), and NRC (1985) along with WACCM4 simulations from Coupe et al. (2019), UR, UR-NO, UR-AOD, UR+NO2, and UR+NO3 (left) and global averages (right) for just the WACCM4 simulations. Kao et al. (1990) only provided information about the end of their 20-day simulation. See Table 1 for the abbreviations and descriptions of the United States/Russia (UR) cases from this study.
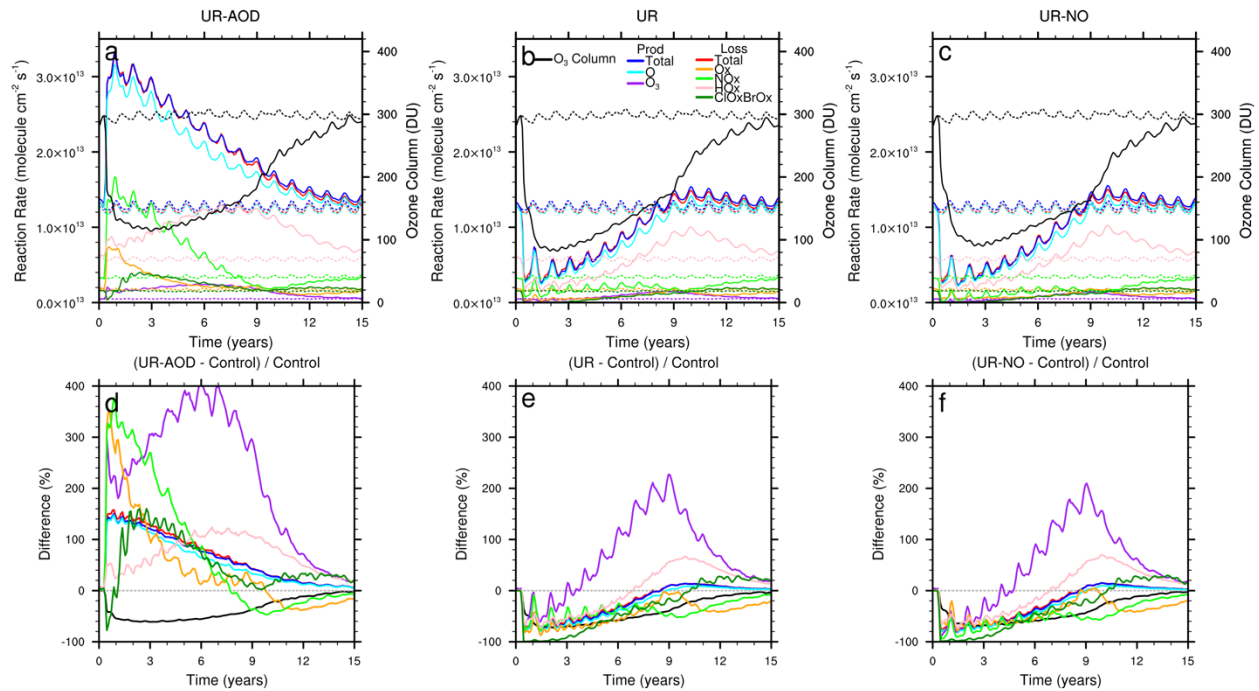
Figure 9. Similar to Figure 3, but for the UR–AOD (left), UR (center), and UR-NO (right) cases.
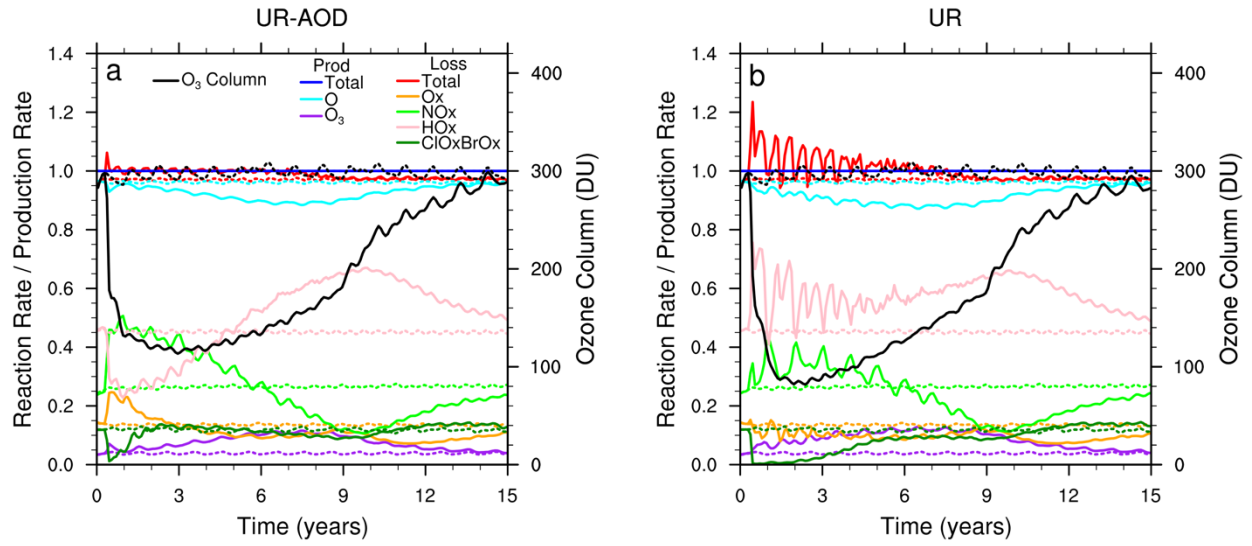
Figure 10. Similar to Figure 4, but for the UR–AOD (left) and UR (right) cases.
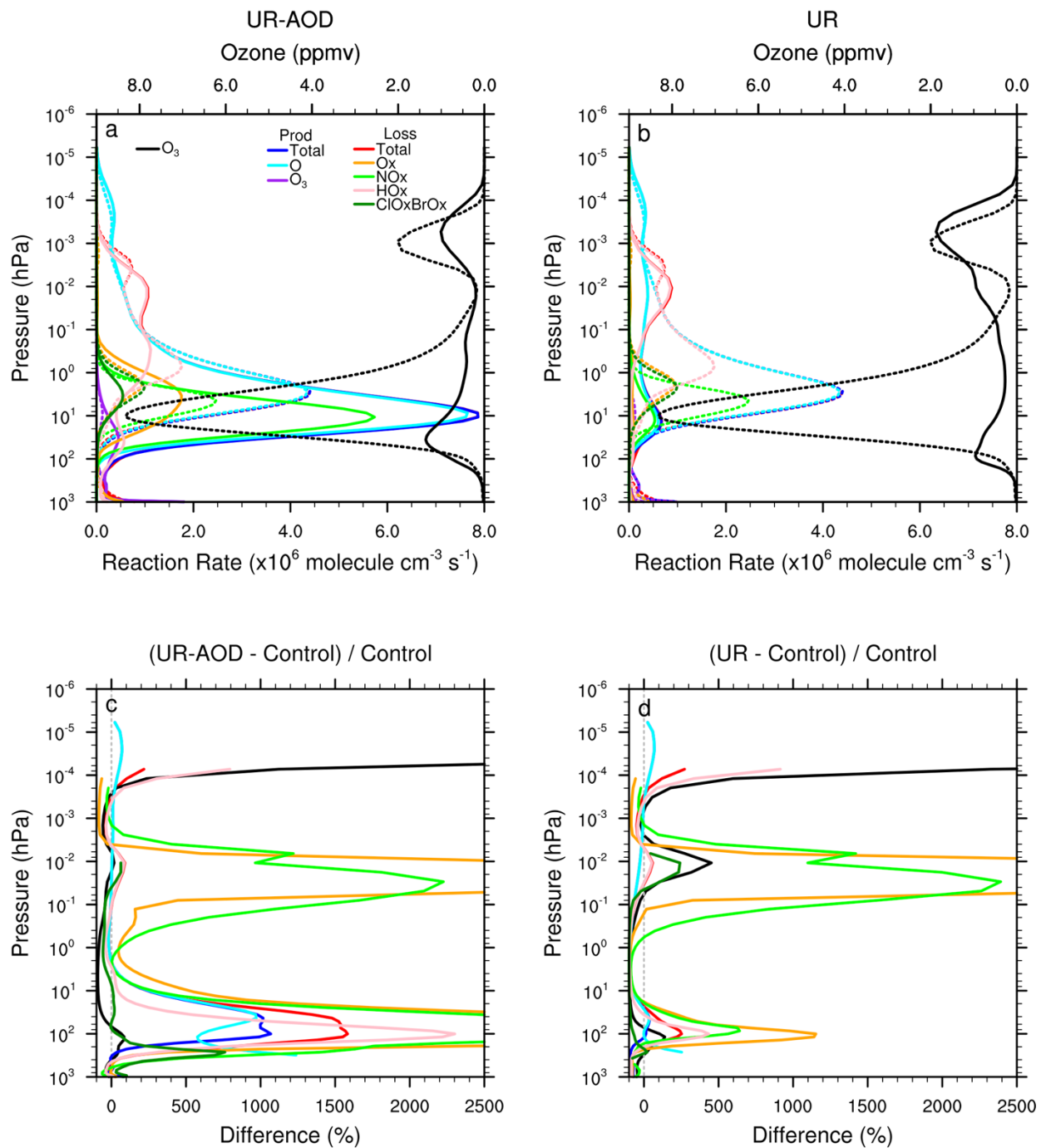
Figure 11. Similar to Figure 5, but for the UR–AOD (left) and UR (right) cases. Note the O₃ scale is increasing toward the left in panels a and b.
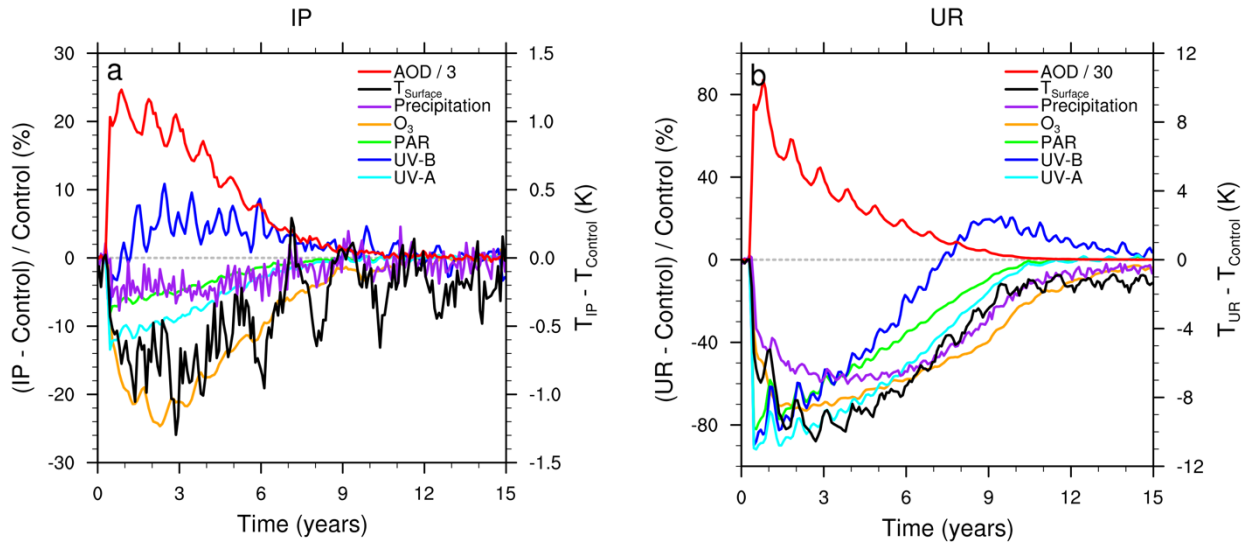
Figure 12. Evolution of the change in the global average for surface values of aerosol optical depth, temperature, O_3 column, and precipitation compared with the spectral integrals of PAR and UV-B for the IP (left) and UR (right) cases. Temperature (black) is on the right scale and the percentage change of the other fields (color) are on the left scale. AOD is the total aerosol optical depth including both the soot and the background aerosol and has been reduced by a factor of 3 in the IP case and 30 in the UR case to fit on the plot. The maximum global average AOD values are 0.13 for the control, 0.20 for the IP case, and 2.92 for the UR case.
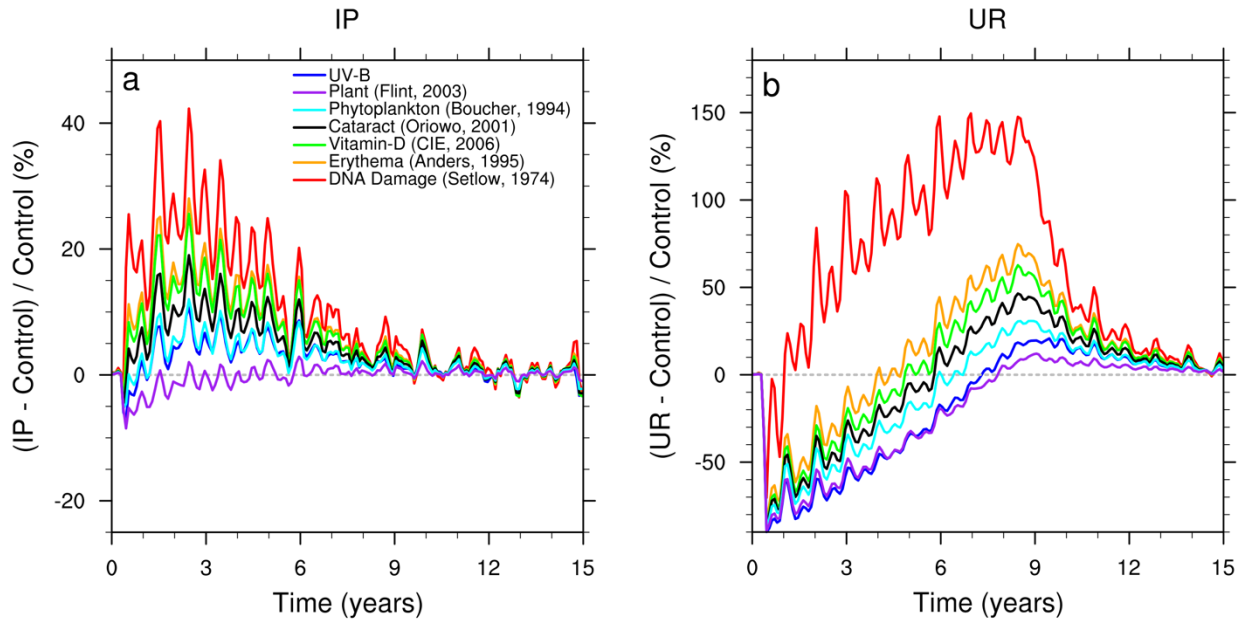
Figure 13. Evolution of the change in the global average surface values for UV-B compared with the action functions for plant growth, inhibition of phytoplankton, cataract formation, vitamin-D synthesis, erythema, and DNA damage for the IP (left) and UR (right) cases. Note the different vertical scales for the two panels.
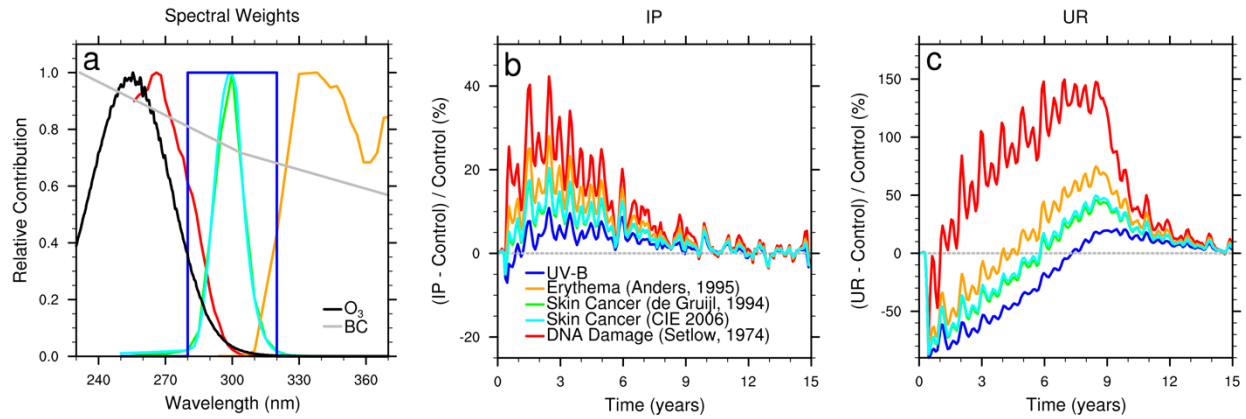
Figure 14. UV spectra for O_3 absorption cross-section (black) and soot mass absorption coefficient (gray) along with spectral weighting functions for UV-B, erythema, DNA damage, and two metrics for non-melanoma skin cancer (colors) over the range 230-370 nm (left). Evolution of the change in the global average spectral integrals of UV-B compared with the action functions for erythema, DNA damage and non-melanoma skin cancer for the IP (center) and UR (right) cases. Note the different vertical scales for these two panels.
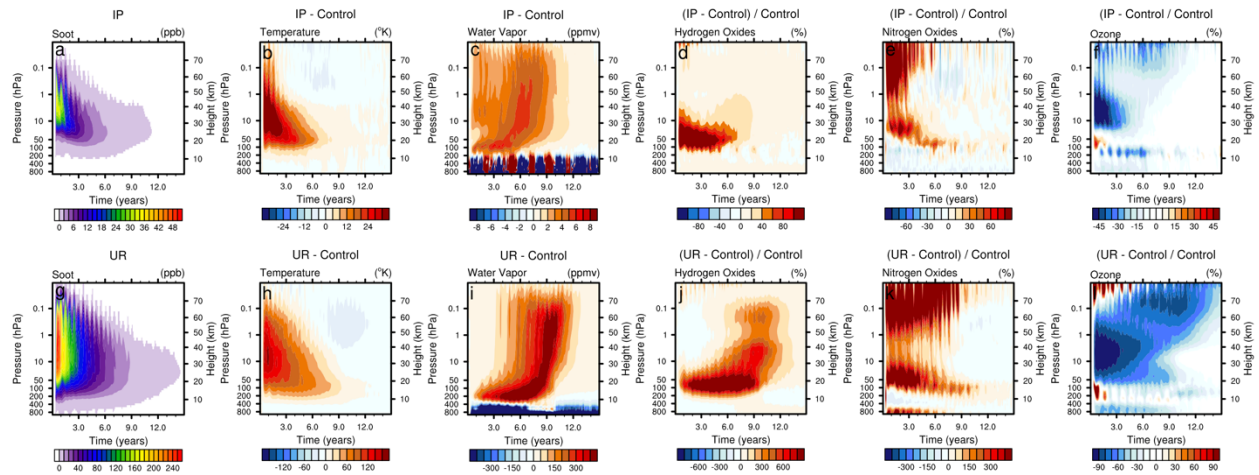
Figure S1. Similar to Figure 1, but with a different scale for the IP case to allow the structure of the IP case to be seen more clearly compared with the UR case. Most UR scales are 5 times the IP scale, except for H_2O which is 50 times and O_3 which is 2 times.
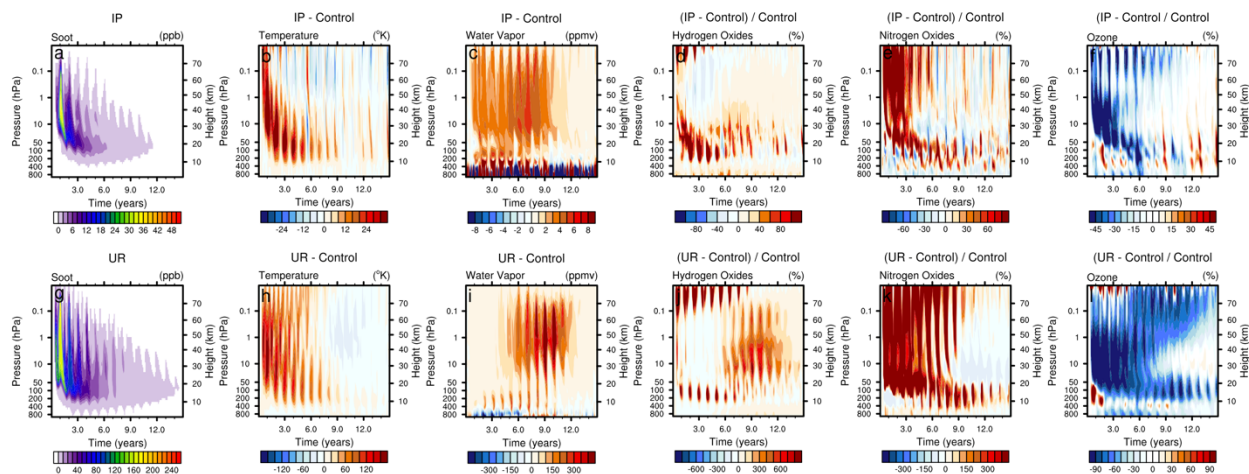
1109

1110
1111   **Figure S2**. Similar to Figure S1, but for the southern polar region (63˚S to 90˚S).
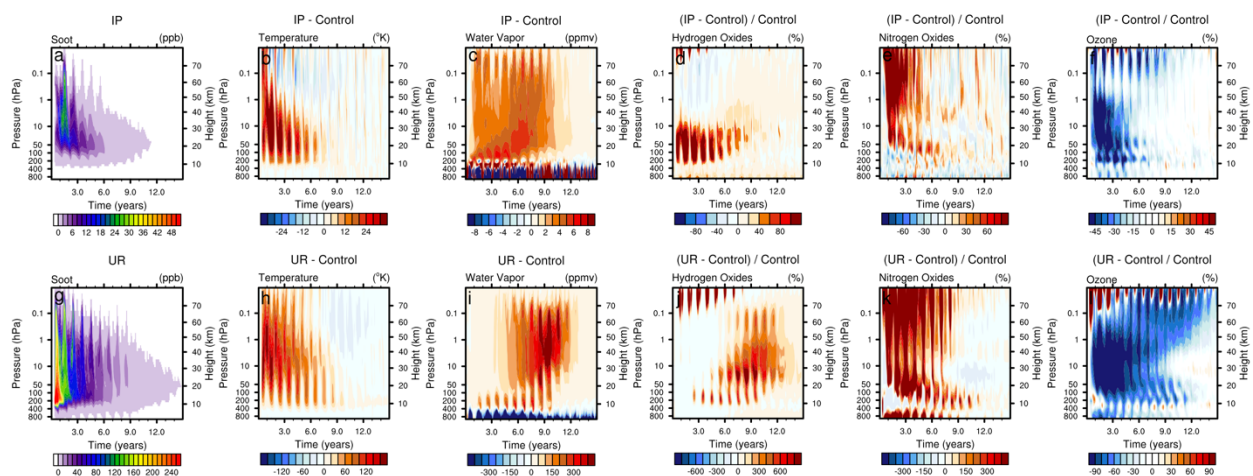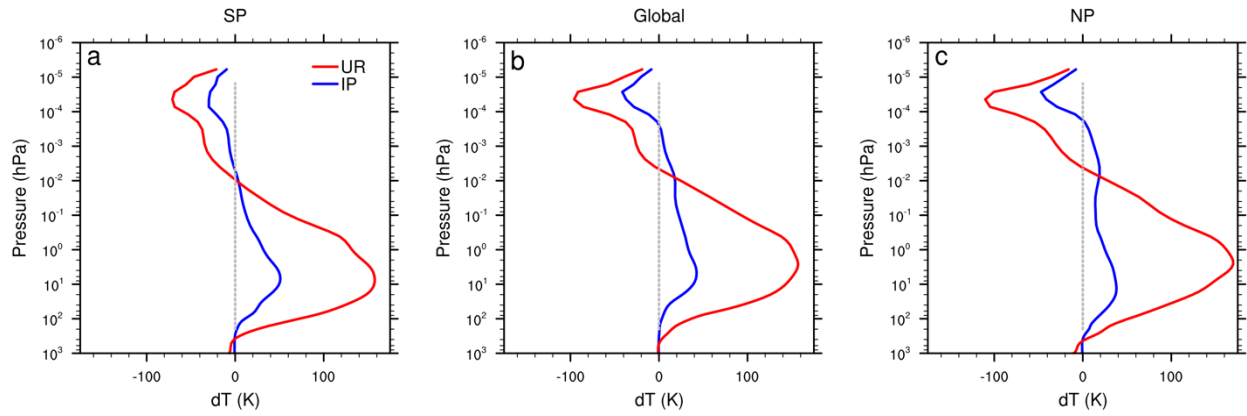1112

1113

1114
1115   **Figure S3**. Similar to Figure S1, but for the northern polar region (63˚N to 90˚N).
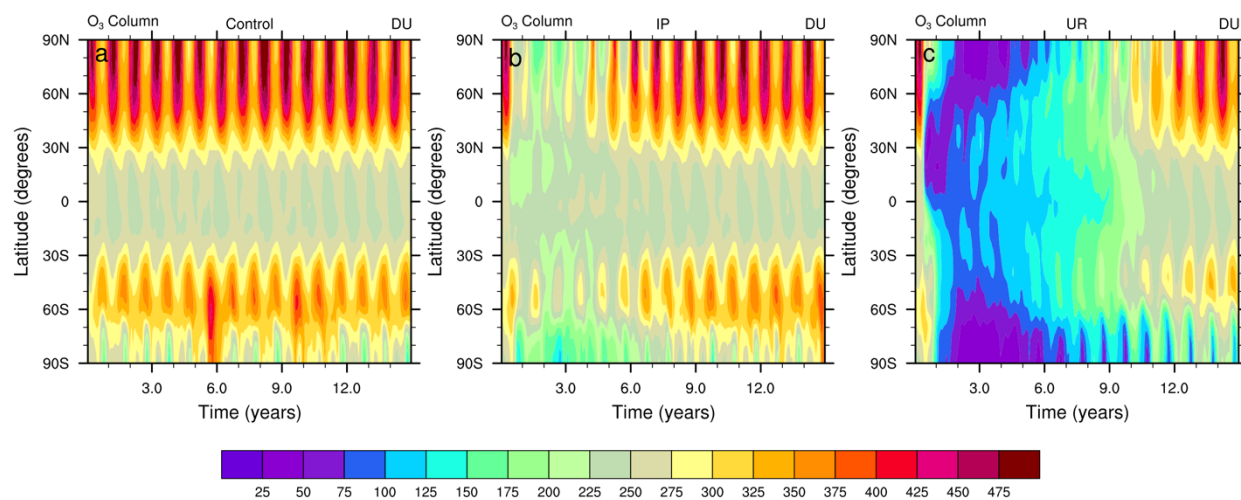1116

Figure S4. Vertical profiles of temperature differences between the IP (blue) and UR (red) cases with the control case for the southern polar (left), global (center), and northern polar (right) averages for the same time period as used in Figures 5 and 11.
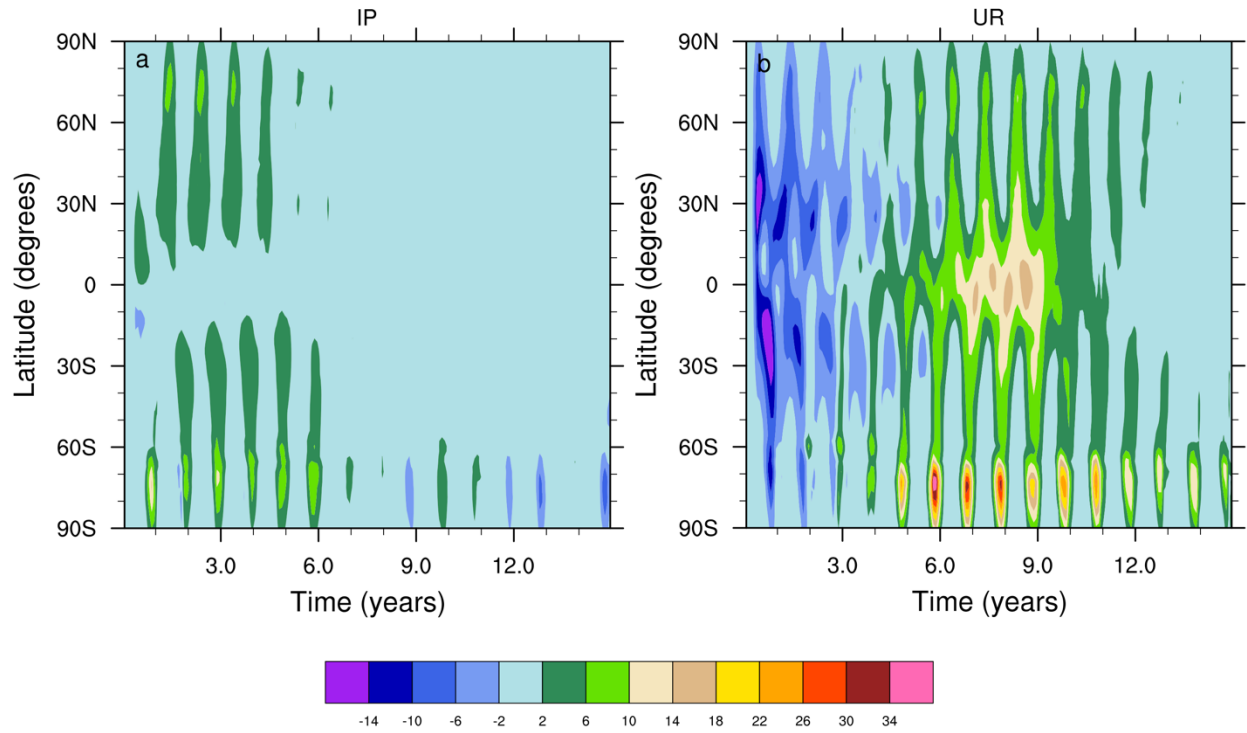
1121

1122
1123 **Figure S5**. Evolution of the zonal monthly column O$_3$ for the control (left), IP (middle),
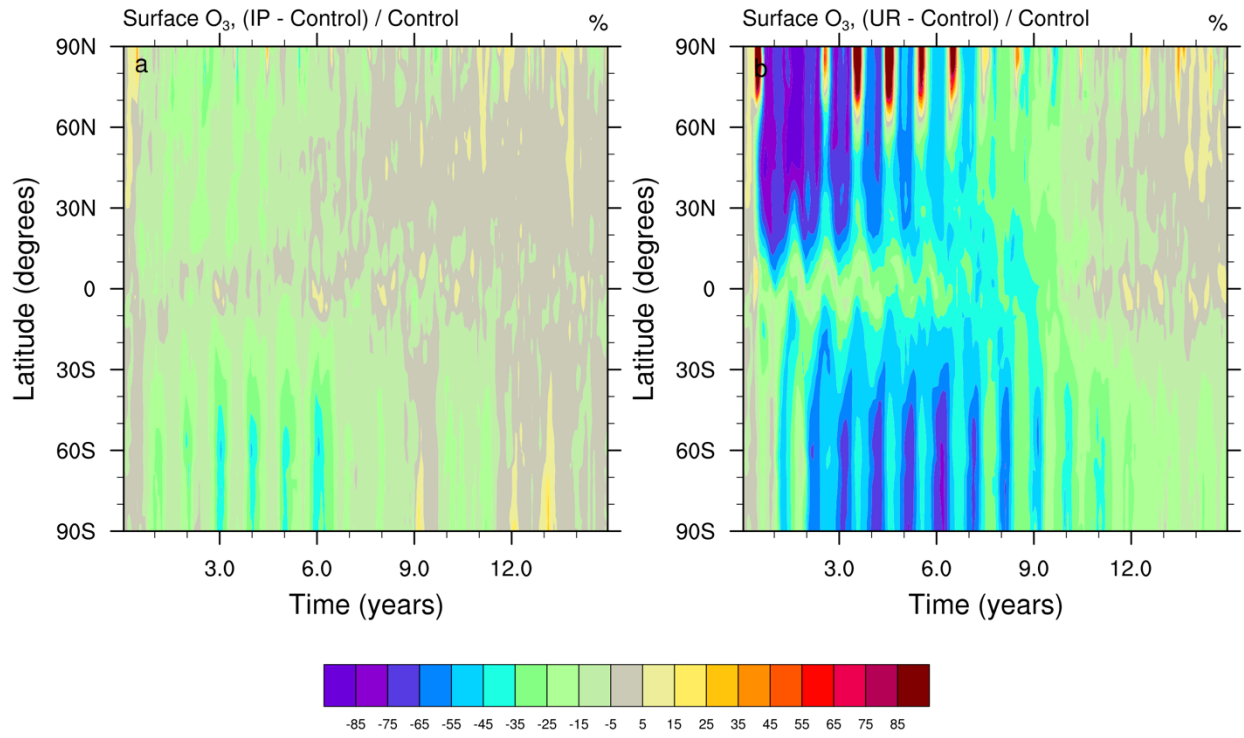1124 and UR (right) cases.

1125

1126
1127

Figure S6. Evolution of the change in zonal and monthly average of the daily maximum UV index for the IP (left), and UR (right) cases.

Surface O₃, (IP - Control) / Control

Surface O₃, (UR - Control) / Control

-85 -75 -65 -55 -45 -35 -25 -15 -5   5   15 25 35 45 55 65 75 85

Figure S7. Evolution of the percentage change in zonal average surface O_3 for the IP (left), and UR (right) cases.
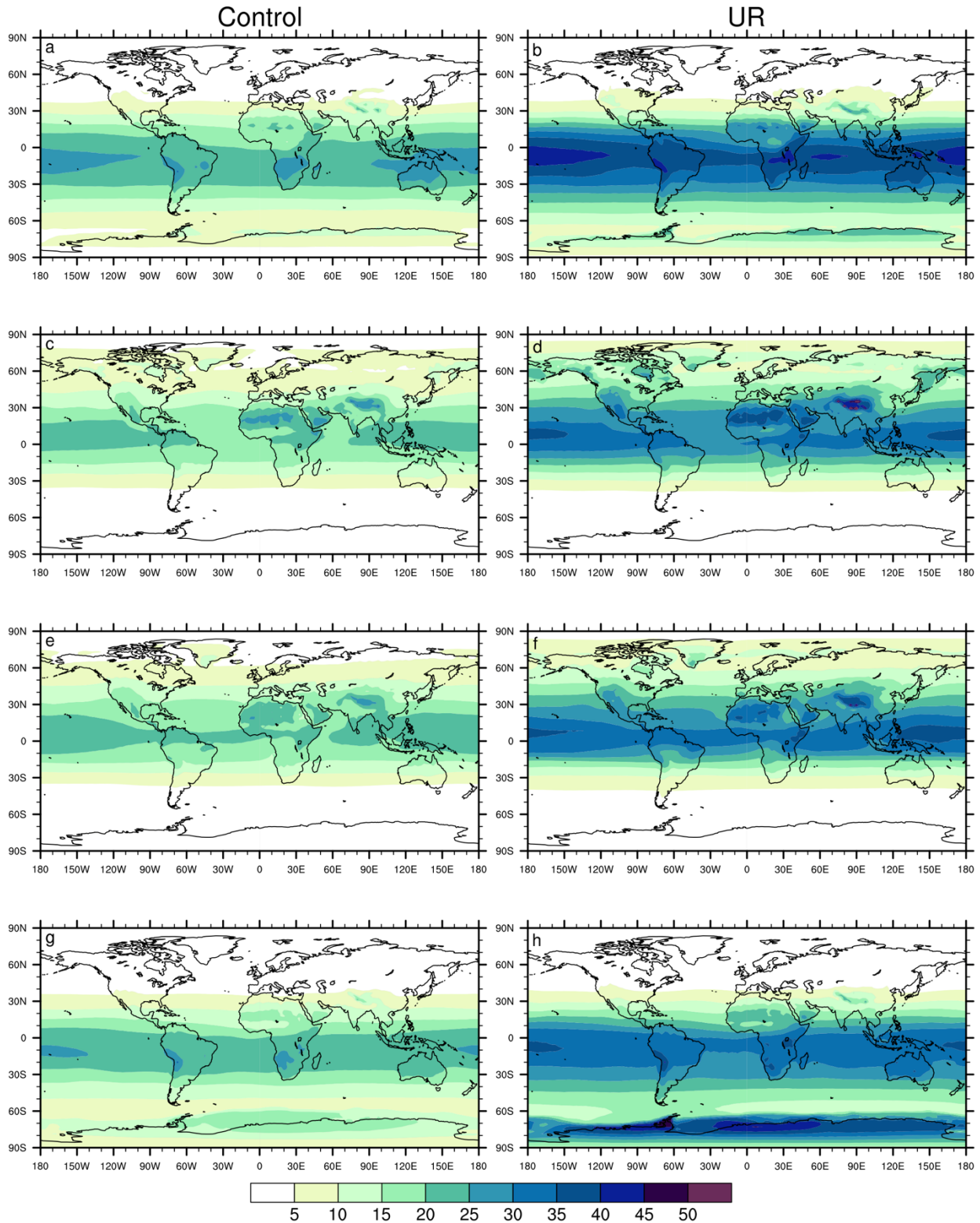
Figure S8. Maps of the monthly average of the daily maximum clear-sky surface UV Index for January (a, b), April (c, d), July (e, f), and October (g, h) averaged from years 8 to 10 for the control (left) and UR (right) cases.

1141

1142

Case	Soot	NO	T	A	Yields (Mt)
Control	0 Tg	0 Tg	X	X	None
Toon et al. (2019)	5 Tg	0 Tg			Total: 0.66 Mt (44x0.015)
IP	5 Tg	0.5 Tg	X	X	Same as above
IP–AOD	5 Tg	0.5 Tg	X		Same as above
IP–NO	5 Tg	0 Tg	X	X	Same as above
Coupe et al. (2019)	150 Tg	0 Tg			None
UR	150 Tg	22.5 Tg	X	X	Total: 1494 Mt (R: 48x0.05, 1232x0.1, 580x0.25, 574x0.8; US: 1486x0.09, 528x0.15, 200x0.3, 600x0.335, 322x0.36, 384x0.455) Kristensen & Korda (2020a; 2020b)
UR–AOD	150 Tg	22.5 Tg	X		Same as above
UR–NO	150 Tg	0 Tg	X	X	None
UR+NO2	150 Tg	21.6 Tg	X	X	Total: 1320 Mt (4400x0.3) Toon et al. (2008) (0.1 Mt → 0.3 Mt)
UR+NO3	150 Tg	39.9 Tg	X	X	Total: 5000 Mt (220x1.5, 2200x1.0, 330x0.75, 1600x0.5, 2400x0.25, 3200x0.1, 12500x0.04) NRC (1985) (no ground bursts)

Table 1. List of the WACCM4/CARMA simulations performed in this study and our prior work. IP indicates a regional conflict between India and Pakistan, and UR indicates a global conflict between the US and Russia. Soot shows the total soot emission, NO the total NO emission (fireball and fire), TUV indicates that in-line TUV was used for photolysis, and AOD indicates that the aerosol optical depth was included in the TUV photolysis calculation. Yields indicate the total yield, the count and size (Mt) of the individual weapons that are assumed for the NO_x production, and the source of the weapon inventory. For Toon et al. (2008), the weapon yield was assumed to be 300 kt rather than 100 kt. For NRC (1985), 1500 Mt of ground bursts were not included in the total. The

1152   different NO emission cases (NO, NO2, and NO3) are sensitivity tests that differ only in
1153   the amount and altitude extent of the fireball NO emission.
1154

Type	Name	Weight	Reactions
Production			
	O	2	$O_2 + h\nu \rightarrow O + O(^1D)$
		2	$O_2 + h\nu \rightarrow 2\,O$
	O_3	1	$NO + HO_2 \rightarrow NO_2 + OH$
		1	$CH_3O_2 + NO \rightarrow CH_2O + NO_2 + HO_2$
Loss			
	O_x	2	$O + O_3 \rightarrow 2\,O_2$
		1	$O(^1D) + H_2O \rightarrow 2\,OH$
	NO_x	2	$NO_2 + O \rightarrow NO + O_2$
		2	$NO_3 + h\nu \rightarrow NO + O_2$
	HO_x	1	$HO_2 + O \rightarrow OH + O_2$
		1	$HO_2 + O_3 \rightarrow OH + 2\,O_2$
		1	$OH + O \rightarrow H + O_2$
		1	$OH + O_3 \rightarrow HO_2 + O_2$
		1	$H + O_3 \rightarrow OH + O_2$
	ClO_xBrO_x	2	$ClO + O \rightarrow Cl + O_2$
		2	$Cl_2O_2 + h\nu \rightarrow 2\,Cl$
		2	$ClO + ClO \rightarrow 2\,Cl + O_2$
		2	$ClO + ClO \rightarrow Cl_2 + O2$
		2	$BrO + ClO \rightarrow Br + Cl + O_2$
		2	$BrO + ClO \rightarrow BrCl + O_2$
		2	$BrO + BrO \rightarrow 2\,Br + O_2$
		1	$BrO + O \rightarrow Br + O_2$
		1	$ClO + HO_2 \rightarrow O_2 + HOCl$
			$BrO + HO_2 \rightarrow HOBr + O_2$

1155 **Table 2.** List of the main chemical reactions used in WACCM that are important to odd-oxygen
1156   (O and O_3) concentrations. These reactions are grouped by production and loss and by
1157   catalytic cycles for analysis purposes. The weight indicates the net odd-oxygen
1158   production or loss from a reaction. These weights are used to sum the individual reaction
1159   rates to calculate total production and loss rates.

1160

1161